

THE ENVIRONMENT AND STRUCTURE OF MASSIVE CENTRAL GALAXIES USING THE SUBARU HYPER SUPRIME-CAM SURVEY

SONG HUANG (黃嵒)¹, HSC COLLABORATION¹

(Dated:)
Draft version 0

ABSTRACT

Although the environmental dependence of structures for massive central galaxies is predicted by the promising hierarchical assembly model, observations at low redshift seem to find no convincing evidence for that. With the help of deep *i*-band images of a large sample of massive central galaxies at $0.3 < z < 0.5$ from the Subaru Hyper Suprime-Cam (HSC) survey, we map their stellar mass distributions out to radius larger than 100 kpc, and discover subtle, but systematic and robust structural differences that depend on halo mass. At fixed stellar mass within 100 kpc, the massive central galaxies in more massive ($M_{200m} > 1.6 \times 10^{14} M_\odot$) halos have a slightly flattened inner profile within $\sim 15\text{--}20$ kpc, and a more prominent outer envelope compared to ones in less massive ($M_{200m} > 8.7 \times 10^{13} M_\odot$) halos. For centrals with $M_* > 10^{11.5} M_\odot$, the ones in more massive halos show very significant excess of mass in the outskirt when the two samples are matched using proxies of mass assembled at $z > 1$. Such differences are broadly consistent with richer recent merging history for more massive halos. We suggest that the relation between total stellar mass and mass within inner 5 or 10 kpc is potentially interesting for diagnosing the role played by host halo in shaping the structures of massive central galaxies. These results also highlight the importance of deep photometry and the usage of detailed structural information in the study of the assembly history of galaxies.

Subject headings: galaxies: elliptical and lenticular, cD — galaxies: formation — galaxies: photometry — galaxies: structure — galaxies: surveys

1. INTRODUCTION

Scientific Background

- Massive galaxies are important cosmic probe and unique labs to study galaxy evolution.
- Briefly explain why massive early-type galaxies are important through the difficulties of stellar-halo mass relation and stellar mass function at the high-mass end.
- Brief summary of the current understanding of their cosmic assembly history.
- Explain why we should care about the environment, and why we expect to see some environmental dependence in the structure and other properties of massive galaxies.
- Brief review of the current observations. It is still not clear whether there is a clear environmental dependence.

Observational difficulties (a.k.a Why we need HSC)

- Explain why it is important to study the mass distribution of massive galaxies out to large physical radius; and, given their unique light profiles, why it is more difficult to study them compared to late-type galaxies.
- Very brief summary of past observational efforts, and why they are not good enough (Not enough number of really massive galaxy; Shallow images; Background subtraction issue; and stacking analysis can be dangerous as while)

song.huang@ipmu.jp

¹ Kavli Institute for the Physics and Mathematics of the Universe, The University of Tokyo Institutes for Advanced Study, the University of Tokyo (Kavli IPMU, WPI), Kashiwa 277–8583, Japan

Basic idea of this work

- Here we take advantages of the ambitious Hyper-Suprime camera survey...

To achieve this goal, we select a large sample of massive central galaxies within halos that are more or less massive than $\log(M_{\text{Halo}}/M_\odot) \sim 14.0$ at $0.3 < z < 0.5$ from the current ~ 100 square degree of HSC data. As indicated by the M_* - M_{Halo} relation, at the same M_* , massive central galaxies with similar morphology can live in halos within large range of M_{halo} , therefore it is very interesting to look into the influence of their halos on the structure of these galaxies. Under the adopted cosmology, $1.0''$ equals 4.4 and 6.1 kpc at redshift 0.3 and 0.5. In this redshift range, we can reliably measure the total stellar mass within the inner 5 to 10 kpc (where the “in-situ” stellar component should dominate) given the typical seeing, while still be able to map their stellar distributions out to ~ 100 kpc at $z \sim 0.5$ given the imaging depth of these HSC data. Also, we can safely ignore significant mass growth and structural evolution (no star formation, lower merger rate et al. e.g. Bellstedt et al. 2016, Inagaki et al. 2015; but also see Bai et al. 2014) with our redshift and M_* ranges.

The paper is organized as follows. Section 2 gives a brief overview of the HSC observation and data reduction, along with the summary of the data selection processes. Then, we will explain the procedures for extracting 1-D surface brightness profiles (Section 3) and estimating stellar mass (Section 4) in details. We will present the main results in Section 5, and discuss the several related technical and scientific issues in Section 6, ending with summary and future plans in Section 7.

All the magnitudes used here are in AB system (Oke & Gunn 1983), and are corrected for Galactic extinction using calibrations from Schlafly & Finkbeiner (2011). In this work,

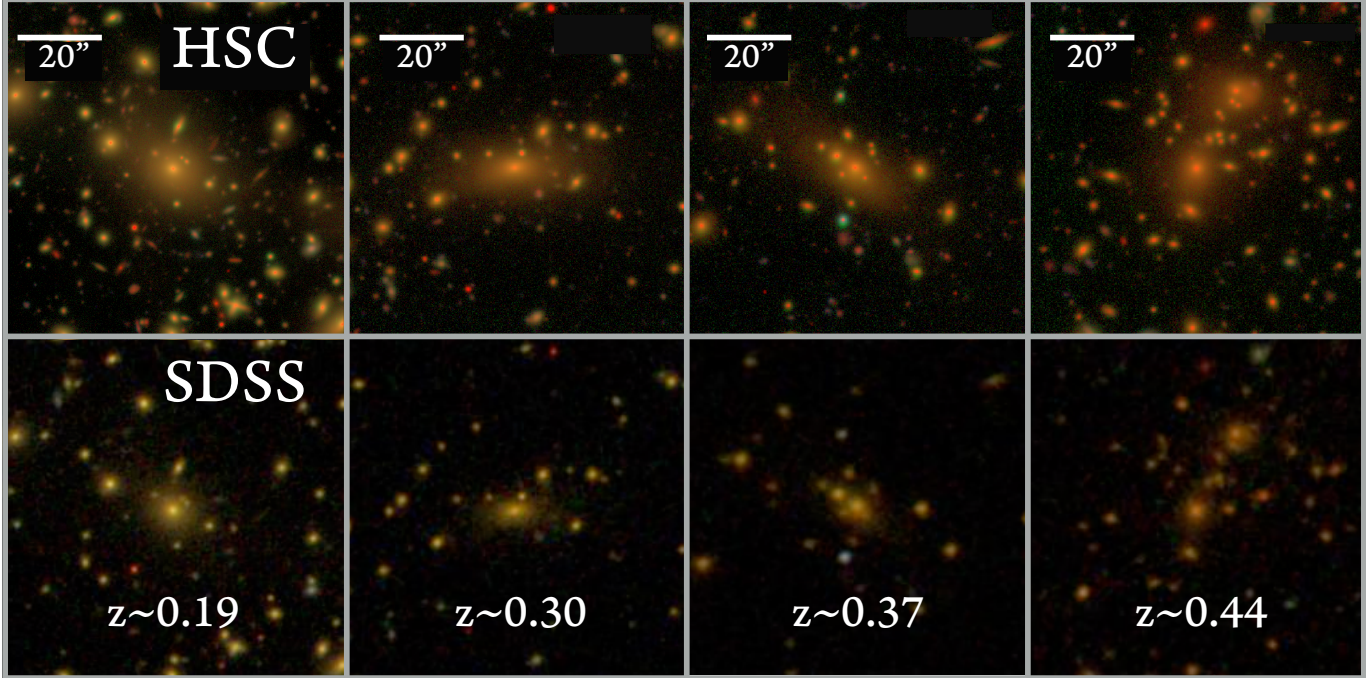


FIG. 1.— A comparison between the imaging quality of SDSS and HSC Wide for a sample of nearby massive elliptical galaxies at $0.2 < z < 0.5$. These images are generated using *gri* band images with an arcsinh stretch (Lupton et al. 2004). The HSC Wide layer is 3.0–4.0 magnitudes deeper than SDSS which is critical in order to map the outskirts of ETGs out to large radii.

we assume $H_0 = 70 \text{ km s}^{-1} \text{ Mpc}^{-1}$, $\Omega_m = 0.3$, and $\Omega_\lambda = 0.7$.

2. DATA AND SAMPLE SELECTION

2.1. The Hyper Suprime-Cam Survey

The Subaru Strategic Program (SSP, REF) makes use of the new prime-focus camera, the Hyper Suprime-Cam (HSC; Miyazaki et al. 2012), on the 8.2-m Subaru telescope at Mauna Kea. This ambitious multi-layer photometric survey takes advantage of the large field of view (FoV; 1.5 deg in diameter) of HSC and will cover $\sim 1400 \text{ deg}^2$ of sky in 5 broad bands ($g\ r\ i\ z\ Y$) to the depth of $r \sim 26$ mag in the WIDE. This work is based on the internal data release S15B, which covers ~ 100 square degree of sky in all 5-band to full WIDE depth. The regions covered by this release overlap with a number of spectroscopic surveys (e.g. SDSS/BOSS: Eisenstein et al. 2011, Alam et al. 2015; GAMA: Driver et al. 2011, Liske et al. 2015).

The HSC WIDE survey is 3.0–4.0 magnitudes deeper in the *i*-band than SDSS. Combined with the excellent imaging resolution (median *i*-band seeing is $0.6''$), and the wide area, this makes the HSC wide layer a tremendous data set to perform a large statistical study of surface brightness profiles of ETGs out to large radii. Fig. 1 illustrated the quality of HSC imaging compared to SDSS for a sample of low redshift ETGs. Fig. 1 clearly demonstrates that the HSC Wide survey is well suited for mapping the stellar distribution of massive galaxies out to large radii and will be a powerful data set to explore the assembly history of ETGs.

The HSC *i*-band images typically have the best seeing in all five bands because of strict requirements determined by weak lensing science. We will therefore use the *i*-band images to measure the stellar distributions of massive galaxies.

2.2. The HSC galaxy catalog and photometry measurements

The HSC SSP data are processed with `hscPipe 4.0.1`, a derivative of the Large Synoptic Survey Telescope (LSST)

pipeline (e.g. Jurić et al. 2015; Axelrod et al. 2010), modified for HSC. `hscPipe` first performs a number of tasks at the single exposure level (bias subtraction, flat fielding, background modeling, object detection and measurements). Then pipeline perform astrometric and photometric calibration for each single exposures. After that, the `hscPipe` warp different exposures on to a common World Coordinate System (WCS), combine them into coadded images with improved signal-to-noise ratio (S/N), and update the images with better astrometric and photometric calibrations at the same time using the common stars among different exposures. The pixel scale of the combined images is $0.168''$. The photometric calibration is based on data from the Panoramic Survey Telescope and Rapid Response System (Pan-STARRS) 1 imaging survey (Schlafly et al. 2012, Tonry et al. 2012, Magnier et al. 2013). To achieve consistent deblending and photometry across all bands, `hscPipe` performs multi-band post-processing at the coadd level. First, the `hscPipe` performs object detection again on the coadd images in each band independently, and identify the above-threshold region (referred as “footprint”) and the flux peak within it for each source. “footprints” and peaks from different bands are then merged together before the `hscPipe` deblend and measure them in each band. Later, `hscPipe` selects a “reference band” for each object based on the S/N in different bands (for most galaxies in this work, it is the *i*-band). After fixing the centroids, shape, and other non-amplitude parameters of each object in this reference catalog, `hscPipe` perform forced photometry on the coadd image in each band. The PSF and galaxy model fluxes measured in the forced photometry approach are the best for color measurements. Please refer to Bosch (in prep.) for more details of the `hscPipe` and the multi-band processing method.

The HSC `cModel` algorithm is similar to the SDSS `cModel` one. It fits the flux distribution of an object using a combination of de Vaucouleur and exponential components after considering the PSF convolution. For more details about

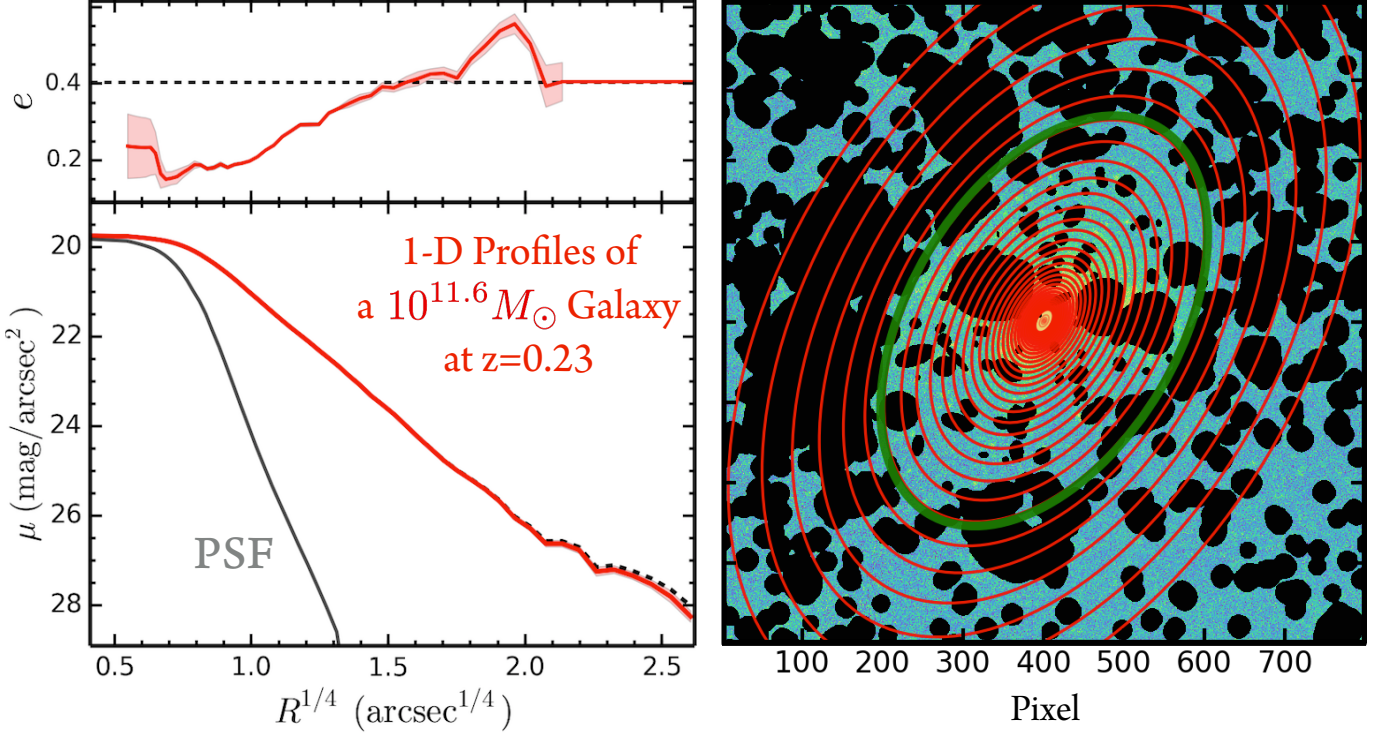


FIG. 2.— Left: example of the 1-D surface brightness and ellipticity profile for a massive galaxy at $z = 0.23$ in i -band using `Ellipse`. In this work, we always show the radial profile in $R^{1/4}$ scale as it is the most appropriate one to show the structural details of massive ETGs at both inner and outer regions. The dash-line shows the surface brightness profile after correcting the background. We also plot the brightness profile of the PSF model normalized at the central surface brightness of the galaxy to highlight the region affected by seeing. On the top panel, the dash line shows the ellipticity used for the final isophote. Right: the masked i -band image of this galaxy with the isophotes extracted by `Ellipse` overlaid. The thick, green isophote highlights the one with $\mu_i \sim 28.5$ mag arcsec $^{-2}$.

the algorithm, please see Bosch et al. in prep.. We have tested its performance using synthetic objects (Huang et al. in prep.), and the results indicate that, generally speaking, the HSC `cModel` photometry is accurate down to $i > 25.0$ mag. However, for massive ETGs with extended stellar distributions, `cModel` currently systematically underestimates their total flux. This problem indicates the intrinsic limitation of `cModel` as it is incapable of modeling profiles that are extremely extended in the outskirt at the depth of HSC survey. At the same time, issues with the deblender also worsen the situation. As the image becomes much deeper, it also significantly increases the fraction objects that are blended with others, and makes reliable deblending process a very challenging problem especially for massive ETGs where satellites and background galaxies often blend with the low surface brightness stellar envelope. To make sure the reliable detection of faint objects close to the detection limit, the deblending method implemented by the `hscPipe` now tends to “over-deblend” the surrounding areas of bright galaxies, and further results in under-estimated total flux of massive ETGs (more discussion in Bosch et al. in prep.). For these reasons, we will perform customized photometric measurements to derive more accurate total luminosity and stellar mass. We only use the HSC `cModel` photometry in the initial selection of parent sample.

2.3. Initial Massive Galaxy Sample

Because of the caveats that apply to `hscPipe` measurements for bright galaxies, we will use custom made software to measure the luminosity profiles of massive galaxies. Our first step is use the HSC galaxy catalog to create an initial sample of massive galaxies that is complete to **XXX** at

$z < 0.5$. We will then use custom made software to re-measure luminosities for all galaxies in this sample. Based on Leauthaud et al. (2016), most $\log(M_*/M_\odot) \geq 11.5$ galaxies should have $i_{\text{SDSS}, \text{cModel}} \leq 21.0$ mag. So we first select all galaxies with $i_{\text{HSC}, \text{cModel}} \leq 21.5$ ² in regions that have reached the required depth of WIDE survey in all five bands.

We select extended objects that have no error in deblending process, well defined centroids, and `cModel` magnitudes in all five bands. After removing the objects that have pixel affected by saturation, cosmic-ray, and other optical artefact³, we select 1760845 galaxies that will be referred as `hscPho`.

As reliable photometric redshift using HSC photometry is still a working progress, we only use objects with either available spectroscopic redshift or robust red-sequence photo-z from the `redMaPPer` catalog (see Section 2.4). We first match the `hscPho` sample with the external spec-z catalog compiled by the HSC database⁴ using $1.0''$ radius. At $0.2 \leq z \leq 0.5$, most redshifts in the HSC spec-z catalog come from SDSS/BOSS and GAMA surveys. The BOSS survey provides the majority of spec-z in this work. Due to the complex selection criteria for different subsamples within the BOSS survey (e.g. the `LOWZ` and `CMASS`), it is not easy to estimate its M_* completeness. Recently, through comparing with the deeper Stripe 82 Massive Galaxy Catalog (S82-MGC; Bundy et al.

² We neglect the insignificant differences between the response curves of SDSS- i and HSC- i filters

³ each criterion affects less than 8% of the entire sample

⁴ It is created by matching HSC objects with public data of several spectroscopic surveys (e.g. SDSS/BOSS; GAMA). Duplicated matches from different sources are merged through internal matching using $0.5''$ radius. For each object, the quality information of the spec-z from different catalogs are homogenized into a single flag that indicates whether the redshift is secure, and only secure spec-z are used in this work.

2015), Leauthaud et al. (2016) suggests that the BOSS spec- z is about 80% complete at $\log(M_*/M_\odot) \geq 11.6$ at $0.3 < z < 0.5$. The GAMA survey, which partially overlaps with the HSC footprint, provides additional 14% unique spec- z . Based on Taylor et al. (2011) (e.g. their Fig. 6), at $z \sim 0.3$, the GAMA sample is 80% complete down to $10^{10.8} M_\odot$; but only 80% complete to $10^{12.0} M_\odot$ at $z \sim 0.5$. Despite the difference in M_* estimates, we can expect our sample should be quite complete above $\log(M_*/M_\odot) \geq 11.5\text{--}11.6$. We will further address the issue of M_* -completeness more carefully using the common sample with S82–MGC (see Section 4.2).

Among the 116813 matched objects, 42696 are at $0.2 \leq z \leq 0.5$. The majority of these redshifts come from either SDSS or BOSS data. GAMA survey contributes another $\sim 14\%$. For objects without external spec- z , we match them with the central galaxies from redMaPPer catalog using $2.0''$ radius. The matched objects with useful red-sequence photo- z (z_λ) are also included in the final sample of bright galaxies with reliable redshift between $0.2 \leq z \leq 0.5$ (will be referred as hscZ). As we will show later (see Section 7.1), to ensure reasonable M_* -completeness at the high- M_* end, and make sure the samples we want to compare have well overlapped redshift distributions, we will focus on the galaxies at $0.3 \leq z \leq 0.5$.

2.4. redMaPPer cluster catalog

In this paper, our study focuses on galaxies which are located at the center of their dark matter halos. To limit our sample to central galaxies, we use v5.10 of the redMaPPer cluster catalog⁵ (e.g. Rykoff et al. 2014; Rozo et al. 2015b). These authors have developed a well-tested red-sequence cluster finder that has been run on SDSS DR8 (Aihara et al. 2011) photometric data. For each cluster, the catalog provides a photometric redshift estimate z_λ , a richness λ , and identified the most likely central galaxy (this is the galaxies with the highest value of the central probability P_{Cen}). A list of member galaxies for each cluster, and associated membership probabilities, is also provided. Details about the performance of the redMaPPer cluster catalog can be found in Rozo & Rykoff (2014), Rozo et al. (2015a), and Rozo et al. (2015b). Several studies have published calibrations between the redMaPPer richness estimate, λ , and halo mass (e.g. Saro et al. 2015; Farahi et al. 2016; Simet et al. 2016). The results of these studies are in good agreement and indicate that clusters identified by redMaPPer ($\lambda > 20$) have $\log(M_{200,c}/M_\odot) \geq 14.0$. Therefore, the redMaPPer catalog helps us group the massive central galaxies into samples with different average M_{halo} . And, to select reliable candidates of central galaxies, we only include the ones with high probability of being the central galaxy ($P_{\text{Cen}} \geq 0.7$).

Although the redMaPPer catalog provides us a good sample of central galaxies in massive halos, the typical uncertainty of λ estimate is still at $\sim 5\text{--}10$ level. In addition, due to the depth and resolution of SDSS images, the redMaPPer catalog becomes slightly incomplete at lower richness ($\lambda < 40$) end at $z > 0.33$. To reduce the impacts from uncertain richness and incomplete selection of massive halos, we will focus on a sample of central galaxies in halos with $\lambda > 30$. This will also help up enhance the M_{halo} contrast in the structural comparison. Based on the calibration in Simet et al. (2016), the $\lambda \geq 20$ sample should have halo mass

(M_{200m}) more massive than $10^{14.0} M_\odot$. For the $\lambda \geq 30$ sample, they should live in halo more massive than $10^{14.2} M_\odot$ using the same calibration. And, we can confirm that the results presented later do not depend on the choice of λ boundary here. For the massive central galaxies that are not in these cluster-level halos, we unfortunately can not estimate their M_{halo} individually, but it is safe to assume they should have $\log(M_{200m}/M_\odot) < 14.0$.

2.5. Massive Central Galaxies from Low and High Mass Halos

Based on recent constraints of M_* - M_{Halo} relation (e.g. Leauthaud et al. 2012, Behroozi et al. 2013, Kravtsov et al. 2014), the M_{halo} of $\log(M_*/M_\odot) > 11.0$ galaxies has a large scatter at fixed M_* . Although we can not yet measure M_{halo} individually, we can still broadly separate them into galaxies in small groups ($\log(M_{\text{Halo}}/M_\odot) < 14.0$) and large groups/clusters ($\log(M_{\text{Halo}}/M_\odot) > 14.0$), and investigate the “environmental”-dependence of their structures.

Firstly, we match the hscZ sample with the massive central galaxies of redMaPPer clusters with $\lambda \geq 20$ and $P_{0.7} \geq 0.7$ using $1.0''$ radius. This step finds 375 matched galaxies at $0.2 \leq z \leq 0.5$ (among them 282 are at $0.3 \leq z \leq 0.5$). We will refer these **central galaxies in more massive halos** as cenHighMh sample from now on. A small fraction of redMaPPer centrals within the HSC footprints are missing due to severe contamination from optical artifacts or bright stars. Spec- z is not available for 67 (17.9%) galaxies in the sample, but their z_λ should be very accurate (median $|z_\lambda - z_{\text{Spec}}|$ is about 0.01 for the ones with spec- z). The median richness (λ) of these clusters is ~ 32 , corresponding to halo mass of $M_{200m} \sim 1.7 \times 10^{14} h^{-1} M_\odot$. Among these central galaxies, 222 are in clusters with $\lambda \geq 30$. When focusing on this subsample, the median richness is ~ 41 , corresponding to halos with $M_{200m} \sim 2.2 \times 10^{14} h^{-1} M_\odot$. Meanwhile, only 15% of cenHighMh sample lives in clusters with $\lambda \geq 50$ ($M_{200m} \sim 3.0 \times 10^{14} h^{-1} M_\odot$). Therefore, the current cenHighMh sample is not dominated by very massive clusters with $M_{\text{halo}} > 10^{15} M_\odot$.

Assuming that the redMaPPer catalog correctly identifies all halos with $M_{200m} \sim 1.0 \times 10^{14} h^{-1} M_\odot$ in the current footprint, the unmatched massive galaxies from the above step should be dominated by central galaxies of less massive halos and massive satellites galaxies. To select a purer sample of massive centrals in $M_{200m} < 10^{14} h^{-1} M_\odot$ halos, we identify and remove any galaxy that is too close to *any cluster member* in redMaPPer catalog in both radius and redshift direction. For each redMaPPer cluster member, we remove objects within a cylinder region around it from the remaining sample. Such cylinder is defined by 1) physical radius of 3.0 Mpc at the red-sequence redshift of the cluster; 2) $|z - z_\lambda| \leq 0.05$ ⁶. Such strict selection will make sure that massive satellites of redMaPPer clusters are removed. At the end of this process, 29973 galaxies remain in the sample (among them, 14532 are at $0.3 \leq z \leq 0.5$). We refer this sample of **central galaxies in $\log(M_{\text{Halo}}/M_\odot) < 14.0$ halos** as cenLowMh later.

However, we should note that the cenLowMh sample at this stage spans a large range in M_* , extending towards

⁵ See: <http://risa.stanford.edu/redmapper/>

⁶ Given that we do not know the accurate redshift of large number of cluster numbers, and the red-sequence redshift still has some uncertainty, we choose to use this very conservative approach to make sure all satellites are removed in the line-of-sight direction at $0.2 \leq z \leq 0.5$

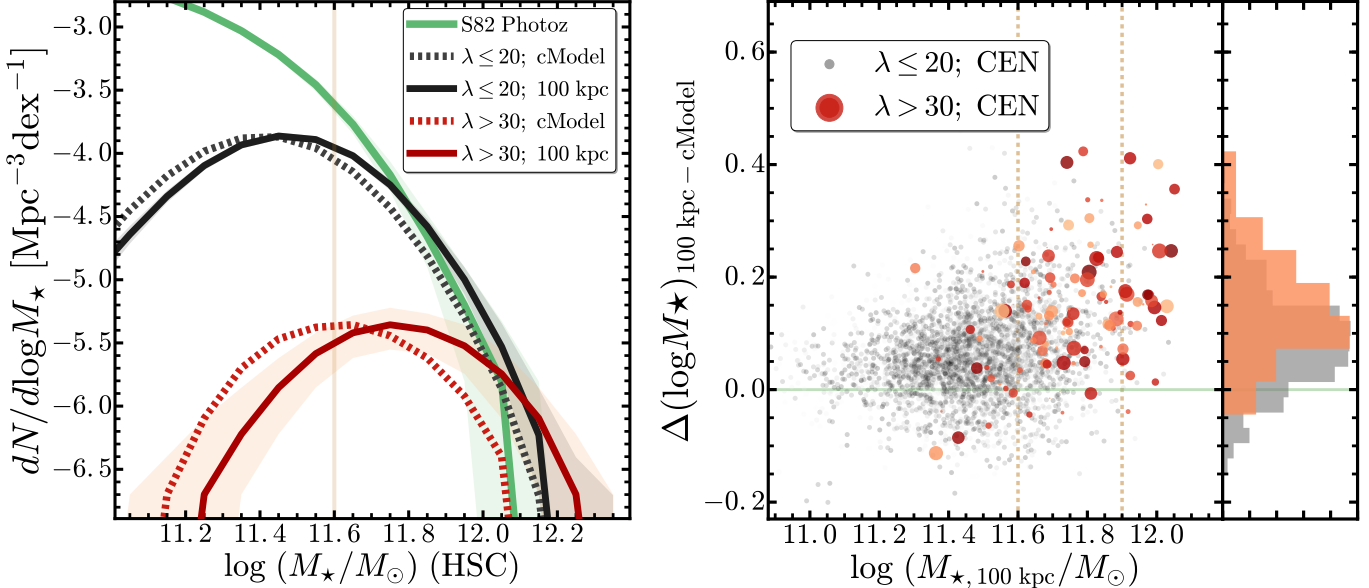


FIG. 3.— **Left:** The M_* volume-density distributions of galaxies at $0.3 < z < 0.5$ for 3) S82–MGC photo- z sample using $M_{*,\text{cModel}}$ (green solid line) along with its uncertainty (green shaded region); 2) cenLowMh ($\lambda \leq 20$; black lines) using both $M_{*,\text{cModel}}$ (dash line) and $M_{*,100\text{kpc}}$ (solid line); 2) cenHighMh ($\lambda > 30$; black lines) using both $M_{*,\text{cModel}}$ (dash line) and $M_{*,100\text{kpc}}$ (solid line). The uncertainties of the distributions for cenHighMh and cenLowMh based on $M_{*,100\text{kpc}}$ are displayed via shaded regions in corresponding colors. The vertical line highlight $\log(M_*/M_\odot) = 11.6$ before correcting the M_* using total luminosity from 1-D profile. Below this value, the cenLowMh sample has relative low completeness. **Right:** comparison of $M_{*,\text{cModel}}$ and $M_{*,100\text{kpc}}$. Since the average M_*/L_* values are the same, the differences here reflect the improvement in photometry through the careful 1-D analysis. We show the cenHighMh sample in solid circles whose color reflects the redshift of the galaxy, and the symbol size suggests the richness of its host cluster. The cenLowMh galaxies are shown in grey dots. Two vertical lines highlight the $11.6 < \log(M_{*,100\text{kpc}}/M_\odot) < 11.9$ mass range where the two samples overlap the most. We also show the histograms of the $\log(M_*/M_\odot)$ differences for galaxies with $11.6 < \log(M_{*,100\text{kpc}}/M_\odot) < 11.9$ using consistent colors.

$\log(M_*/M_\odot) < 10^{11}$. Therefore, we should expect contamination from satellites in $\log(M_{\text{Halo}}/M_\odot) < 14.0$ halos at certain degree. Later, after we update the total M_* of them, we will mainly focus on the cenLowMh galaxies at high mass end, especially the ones at $\log(M_*/M_\odot) > 11.5$. Based on observational constraints (e.g. van Uitert et al. 2016), we can neglect satellite contamination at such high M_* range.

2.6. Summary of Sample Construction

In summary, from the $\sim 100 \text{ deg}^2$ deep HSC images, we select a large sample of massive central galaxies with reliable redshift information, and broadly separate them into two groups with different M_{halo} . To help you go through the results, here are a few key points to keep in mind:

- **hscPho sample:** this parent sample consists of bright galaxies with $i_{\text{cModel}} \leq 21.0$, good quality images and reliable **cModel** photometry in all five HSC bands in the S15B data release.
- **hscZ sample:** through matching the **hscPho** sample with spectroscopic redshifts from surveys like SDSS/BOSS and GAMA, or accurate red-sequence photometric redshift in the **redMaPPer** catalog, we come up with a large sample of bright galaxies with reliable redshift information.
- **cenHighMh sample:** we select a sample of 375 galaxies at $0.2 \leq z \leq 0.5$ that are identified as central galaxies in $\lambda > 20$ **redMaPPer** clusters. The most reliable ones ($P_{\text{Cen}} > 0.7$) among them will represent the central galaxies in very massive halos ($\log(M_{\text{Halo}}/M_\odot) \geq 14.0$).
- **cenLowMh sample:** after excluding all the galaxies that are close to any **redMaPPer** clusters in both radial

and redshift directions from the **hscZ** sample, we have 29973 bright galaxies at $0.2 \leq z \leq 0.5$. With the help of M_* estimates via SED fitting (see Section 4.1), we consider the massive ones among them as the candidates of central galaxies in halos with $\log(M_{\text{Halo}}/M_\odot) < 14.0$.

- To compare the **cenHighMh** and **cenLowMh** samples carefully, we will focus on the redshift range at $0.3 \leq z \leq 0.5$ where their redshift distributions greatly overlap and both samples have acceptable M_* -completeness (see Section 4.2). Also, during the comparison of structures, we will mainly use **cenHighMh** galaxies with $\lambda > 30$ to ensure that they are from more massive halos than the ones in **cenLowMh** sample.

3. MEASUREMENTS OF 1-D SURFACE BRIGHTNESS PROFILE

To estimate the total luminosity of massive galaxies, and measure their one-dimensional stellar mass density (μ_*) profiles, we perform elliptical isophotes fitting using the IRAF task **Ellipse** (Jedrzejewski 1987). Compared to the popular two-dimensional model fitting method, the isophote fitting approach is much less sensitive to the choice of model, number of components, and the initial guesses of free parameters. It is also less affected by the uncertainty of sky background subtraction. This is particularly important for the massive ellipticals in our sample. The much deeper HSC image reveals significantly more extended structures, while also make it inappropriate to fit these galaxies with simple model like the de Vaucouleurs model or single Sérsic component model. Such models fail to fit the central region and the stellar halo of massive galaxies simultaneously, and also can not account for the radial variation of ellipticity and position angle. In principle, such massive galaxies can still be described using more complex models (e.g Huang et al. 2013b; Huang et al. 2013a). However, they are still very sensitive to background subtrac-

tion. And it becomes even more difficult to choose initial parameters, and investigate the degeneracies among parameters. Although it is certainly worth exploring in the future, we decide that the 1-D method suits the goal of this work better.

We first prepare large i -band cut-out images around these massive galaxies that cover at least 750 kpc in radius, along with the bad pixel masks, and the PSF model reconstructed using the central coordinates. While they include all the visible light of the galaxy, they also leave enough space to evaluate the background subtraction. We choose to use i -band images not only considering their excellent seeing condition, but also because they trace the stellar distributions of massive galaxies at $0.3 \leq z \leq 0.5$ reasonably well (fall between rest-frame g and r band), and they suffer less from background uncertainty, which is crucial for studying the outskirt of massive ETGs. Although z and Y-band should be better μ_* tracer, the sky background is much higher and the seeing is considerably worse on average.

Secondly, using the SEP Python library, we perform SExtractor-like background estimation and object detections using different configurations to overcome the “over-deblending” challenge met by the hscPipe. Combining detections using different backgrounds and S/N thresholds, we correctly obtain the footprints of all objects, even of the ones that are very close to the center of bright galaxies. For the rest objects, we convert their footprints into a mask image for the Ellipse procedure after increasing their sizes adaptively based on the brightness and distance to the massive galaxy. We achieve this via convolving the individual footprint with a Gaussian kernel so that we can conservatively exclude pixels affected by this object while still making the mask follow the shape of the object. Meanwhile, we create a more aggressive mask of *all* objects in the same approach, median-rebin the remaining pixels using a 6×6 pixels box, and take the peak value (or mode) of the distribution of these rebinned “sky” pixels as the average background value around these bright galaxies. As expected, we often found slightly negative value that indicate over-subtraction of background at certain degree. In hscPipe, the background on each CCD is modeled with a Chebyshev-polynomial fit to the smoothed image after excluding pixels with $S/N > 5$. This algorithm suffer less than the SDSS version (e.g. see Blanton et al. 2011), but still over-subtract background around very bright object. For our massive galaxies, such over-subtracted background creates artificial truncation or steeper surface brightness profile. We therefore provide an ad hoc fix using a SExtractor-style background model (200×200 pixels background box size, and 6 pixels median filtering size of sky boxes) via running SEP on the image with all objects masked out. This model can account for the slightly over-subtracted background at very large scale, shift the distribution of rebinned “sky” pixels to 0, and do not affect the intrinsic flux distribution of our target.

Finally, we run Ellipse on the background-corrected image following similar strategy of (Li et al. 2011). In short, we start with free centroid and shape of each isophote, then gradually constrain their behaviors, and eventually extract 1-D surface brightness profile along the major axis using isophotes with fixed centroid and shape. The 4th Fourier modes are included to fit the isophote better. In this way, we can extract the radial changes of the centroid, ellipticity, position angle, and average isophotal distortions (more “disky” or “boxy”, e.g. Kormendy et al. 2009) along with the surface brightness profile. Fig. 2 shows an example of the 1-D surface brightness and ellipticity profile for a massive galaxy at $z \sim 0.2$ along

with its masked image and a subset of isophotes. Appendix A includes more details about the Ellipse procedure.

For physical (e.g. late-stage major merger) and unphysical (e.g. nearby foreground galaxy or bright star) reasons, we can not extract reliable 1-D profiles for small fraction of massive galaxies due to heavily masked out central region. This issue reflects an intrinsic limitation of the 1-D method. It affects 48/375 cenHighMh galaxies, and a smaller fraction of cenLowMh ones. It is worth noting that this excludes most massive galaxies in major merger process from the analysis. We will come back to them in the future using 2-D modeling method.

We correct these surface brightness profiles for Galactic extinction and cosmological dimming, then integrate them to various radius to get the luminosity within different physical apertures. Although the i -band 1-D profile can in principle reach to ~ 30 mag arcsec $^{-2}$, we notice the profiles at very low surface brightness part are often less reliable by showing truncation or large fluctuation that are due to either background uncertainty or contamination from bright neighbours. We therefore only consider the < 28.5 mag arcsec $^{-2}$ part of the profile here. This conservative choice already allows us to study the region out to ~ 120 kpc for massive galaxies in this sample.

4. STELLAR MASSES AND STELLAR MASS DENSITY PROFILES

4.1. Stellar Masses from SED Fitting

To convert the luminosity into stellar mass estimates, we assume that these massive galaxies can be well described by an average M_*/L_* . This is a reasonable assumption considering that they are ETGs that are dominated by old stellar population and are known to have shallow color gradients. We will further justify this point using the average color profiles in Section 6.

We use the broadband Spectral Energy Distributions (SEDs) fitting (see Walcher et al. 2011 for a recent review) code iSEDFit⁷ (Moustakas et al. 2013) to estimate the average M_*/L_* and k -corrections using 5-band HSC cModel fluxes under forced-photometry mode. Although cModel tends to underestimate the total flux for bright, extended objects, the forced-photometry results still provides accurate *average* color of the galaxy as it constrains the behaviour of the model using the optimized reference one and takes the PSF convolution into account (e.g. Huang et al. in prep.).

iSEDFit takes a simplified Bayesian approach. In short, it first generates a large grid of SEDs from synthetic stellar population models by drawing randomly from the prior distributions of relevant parameters (e.g. age, metallicity, dust extinction, and star formation history). Based on these models, it uses the observed photometry and redshift to compute the statistical likelihood, and generate the posterior probability distribution (PDF) functions of each parameter. To get the best estimate of certain parameter, iSEDFit “integrates” the full PDF over all the other “nuisance” parameters. Then, the median value of the resulting marginalized PDF is used as the best value, while the $1-\sigma$ uncertainty is derived from the cumulative PDF. Please refer to Moustakas et al. (2013) for technical details and performance of iSEDFit.

In this work, we derive average M_*/L_* using the Flexible Stellar Population Synthesis⁸ (FSPS; v2.4; Conroy & Gunn

⁷ <http://www.sos.siena.edu/jmoustakas/isefit/>

⁸ <http://scholar.harvard.edu/cconroy/sps-models>

2010a, Conroy & Gunn 2010b) model based on the MILES⁹ (Sánchez-Blázquez et al. 2006, Falcón-Barroso et al. 2011) stellar library and Chabrier (2003) IMF between 0.1 to 100 M_{\odot} . We use a delayed- τ model with stochastic star burst as the form of star formation history (SFH), and choose a set of reasonable parameters after some tests. Such form of SFH is appropriate for massive galaxies at low redshift (e.g. Kauffmann et al. 2003). For stellar metallicity, we assume flat distribution between 0.004 to 0.03 (which is the highest metallicity allowed by FSPS models). And, we adopt the Calzetti et al. (2000) extinction law with a order two Gamma distribution of A_V between 0 to 2 magnitude. Since most galaxies in both samples are red, quiescent galaxies, the results are not very sensitive to parameters related to SFH and internal dust extinction. To achieve reasonable sampling across these parameters, we generate 250000 models.

We construct five band SED using the forced-photometry cModel magnitude corrected for the Galactic extinction. As for the photometric error, the current cModel photometry underestimates the flux errors of bright galaxies as it only includes statistical error, not the systematic uncertainties in the model-fitting process. From tests of synthetic objects, we find that the average accuracy of cModel photometry for bright galaxy is roughly at 1% level. Therefore, we supply iSEDFit with simplified flux errors assuming $S/N = 100$ for riz bands, and $S/N = 80$ for gY bands (on average, images in gY bands are shallower in depth and/or have higher background noise). The typical uncertainty of $\log(M_{\star}/M_{\odot})$ for both samples is around 0.08-0.10 dex at the high- M_{\star} end. Please see Appendix B for more detailed discussions of the SED fitting results.

4.2. Comparison with S82-MGC

Given the heterogeneous nature of the redshift resources for these samples, we further investigate their M_{\star} completeness via comparing with galaxies that are in common with the S82-MGC sample. The S82-MGC sample matches the deeper SDSS photometric data in the Stripe 82 region (Annis et al. 2014) with the near infrared data from the United Kingdom Infrared Telescope Infrared Deep Sky Survey (UKIDSS; Lawrence et al. 2007). The deeper photometry and better photo-z make the S82-MGC sample complete to $\log(M_{\star}/M_{\odot}) \geq 11.2$ at $z < 0.7$.

The match between the hscPho sample and the S82-MGC one results in 20453 galaxies at $0.3 \leq z \leq 0.5$ (referred as s82Pho sample). We estimate their M_{\star} using cModel SED in exactly the same way. The M_{\star} using HSC photometry shows tight correlation with ones based on the S82-MGC SED (five optical bands from SDSS and NIR data from UKIDSS; and S82-MGC also used iSEDFit under slightly different assumptions). Then we estimate the volume densities distributions of galaxies in cenHighMh, cenLowMh, and s82Pho samples (left panel of Fig.3) using rough estimates of the survey areas they occupied (since we only care about the relative shapes of the density distributions). And, we estimate the uncertainties of these distributions using a 10000 times bootstrap resampling. The distribution of cenLowMh sample starts to deviates from the s82Pho one below $\log(M_{\star}/M_{\odot}) < 11.6$, indicating that the sample starts to become incomplete within $0.3 \leq z \leq 0.5$. As for the cenHighMh sample, their mass completeness should be bet-

ter thanks to the reliable redMaPPer z_{λ} . Its behaviour is quite consistent with the mass function of galaxies in massive halos with a narrow M_{halo} distribution (REF). Later, we will see that the cModel photometry on average underestimate the M_{\star} of galaxies with $\log(M_{\star}/M_{\odot}) > 11.5$ by -0.1 dex. Therefore, we conclude that the cenLowMh becomes not perfectly complete below $\log(M_{\star}/M_{\odot}) < 11.7$. This is most likely due to the incompleteness of the BOSS spec-z sample. Although it is unlikely that the incompleteness will bias the results of our comparisons, we will bear this in mind, and match the two samples carefully in $\log(M_{\star}/M_{\odot})$ and redshift space before comparing them.

4.3. Stellar Mass Corrected for Total Luminosity

Using the best-fit stellar mass from iSEDFit (referred as $M_{\star,\text{cModel}}$), we estimate the average M_{\star}/L_{\star} in i -band, then use that M_{\star}/L_{\star} to convert the 1-D luminosity density profiles into stellar mass density profiles; and also convert the luminosity within 10 and 100 kpc apertures into corresponding stellar mass estimates (referred as $M_{\star,10\text{kpc}}$ and $M_{\star,100\text{kpc}}$). From now, we use $M_{\star,100\text{kpc}}$ as the new proxy of “total” stellar mass of these galaxies. And we also derive the k -corrected luminosity and colors from the results. In Appendix B, we also show the outputs like the average stellar age, metallicity, and internal dust extinction all behave reasonably for both samples, but will not use them for further scientific analysis.

As expected, the integration of 1-D profile out to very large radius help recover more luminosity (stellar mass) compared to the cModel results. We highlight this in the right panel of Fig.3 as we show the distributions of differences between $M_{\star,100\text{kpc}}$ and $M_{\star,\text{cModel}}$, and their relations to the $M_{\star,100\text{kpc}}$. For both samples, we see the “extra mass” recovered by 1-D photometry increases with $M_{\star,100\text{kpc}}$, therefore this improvement impacts the cenHighMh sample more. This is basically consistent with the fact that the structure of massive ETGs depends on its stellar mass in a way that more massive ones tends to be more extended (e.g. REF). Apparently, such mass-dependent difference between $M_{\star,100\text{kpc}}$ and $M_{\star,\text{cModel}}$ will result in difference of the SMF. As the slope and normalization of SMF at high mass end is very sensitive to both cosmology and interesting baryonic processes such as AGN feedback (REF), they are particularly important in constraining the galaxy evolution model, and therefore became the center of some intense arguments (REF). Although the jury is still out on this topic, it has become clear that popular results using SDSS photometry (REF) underestimate the total luminosity (stellar mass) of massive ETGs. However, past works (e.g. REF) often relied on either stacking of shallow images or the extrapolation of models to investigate this effect. Using the deep HSC images, we have the potential to answer this question much better. Detailed studies of SMF deserves more careful investigations of many systematic issues (e.g. REF), so we just show the impact of the “extra mass” on the volume density distributions of both samples (Fig.3, left panel). Generally speaking, the stellar mass corrected for total luminosity shifts the distribution toward the higher mass end, and slightly modify the slope. People who want to use HSC photometry or other cModel-like photometry to study the properties and evolution of SMF should be aware of such effect.

As mentioned earlier, our assumption of using an average M_{\star}/L_{\star} ignores its radial variation. It is well known that massive ETGs have negative optical color gradient which indicates a gradient of M_{\star}/L_{\star} (e.g. La Barbera et al. 2012; D’Souza et al. 2015), but the gradient is smooth and shallow

⁹ <http://www.iac.es/proyecto/miles/pages/stellar-libraries/miles-library.php>

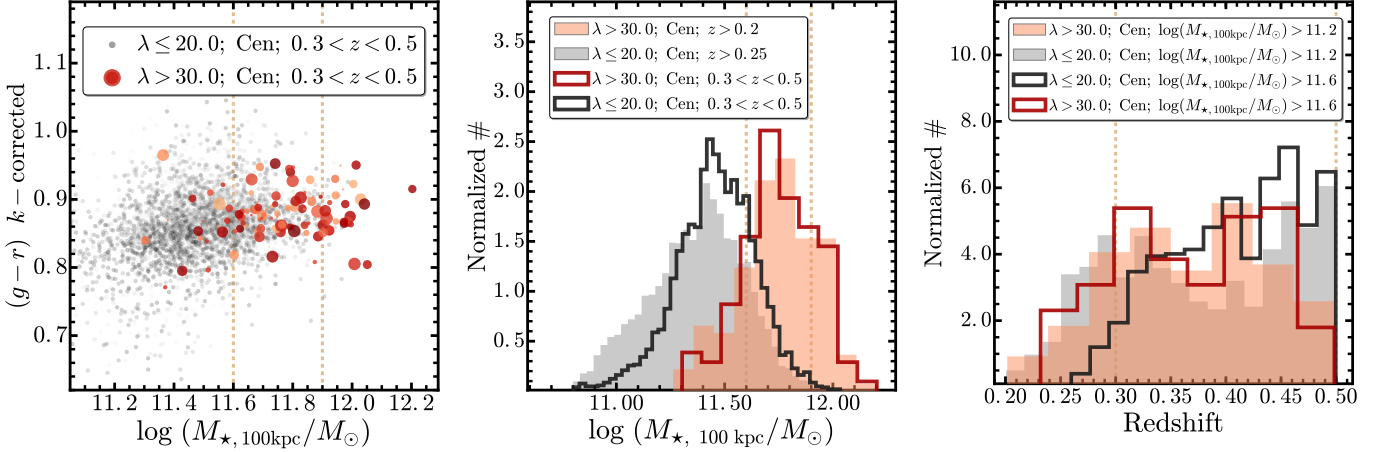


FIG. 4.— **Left:** The $\log(M_*/M_\odot)$ - $g-r$ color relation of the cenHighMh (red circle; datafield format is the same with the right panel of Fig.3) and cenLowMh (grey dots) samples. We apply the k -corrections from `iSEDFit` fitting to the colors. **Middle:** the histograms of $M_{*,100\text{kpc}}$ for the cenHighMh (orange-red) and cenLowMh (grey-black) samples at both $z > 0.2$ (step-filled histogram) and $0.3 \leq z \leq 0.5$ (stepped histogram). The vertical lines in both left and middle figures highlight the $11.6 < \log(M_{*,100\text{kpc}}/M_\odot) < 11.9$ mass range that will be used in the comparison of the $M_{*,100\text{kpc}}$ -matched samples. **Right:** the histograms of the redshift for the cenHighMh and cenLowMh galaxies in both $\log(M_{*,100\text{kpc}}/M_\odot) > 11.2$ and $11.6 < \log(M_{*,100\text{kpc}}/M_\odot) < 11.9$ mass bins. The vertical lines highlights the $0.3 \leq z \leq 0.5$ redshift range.

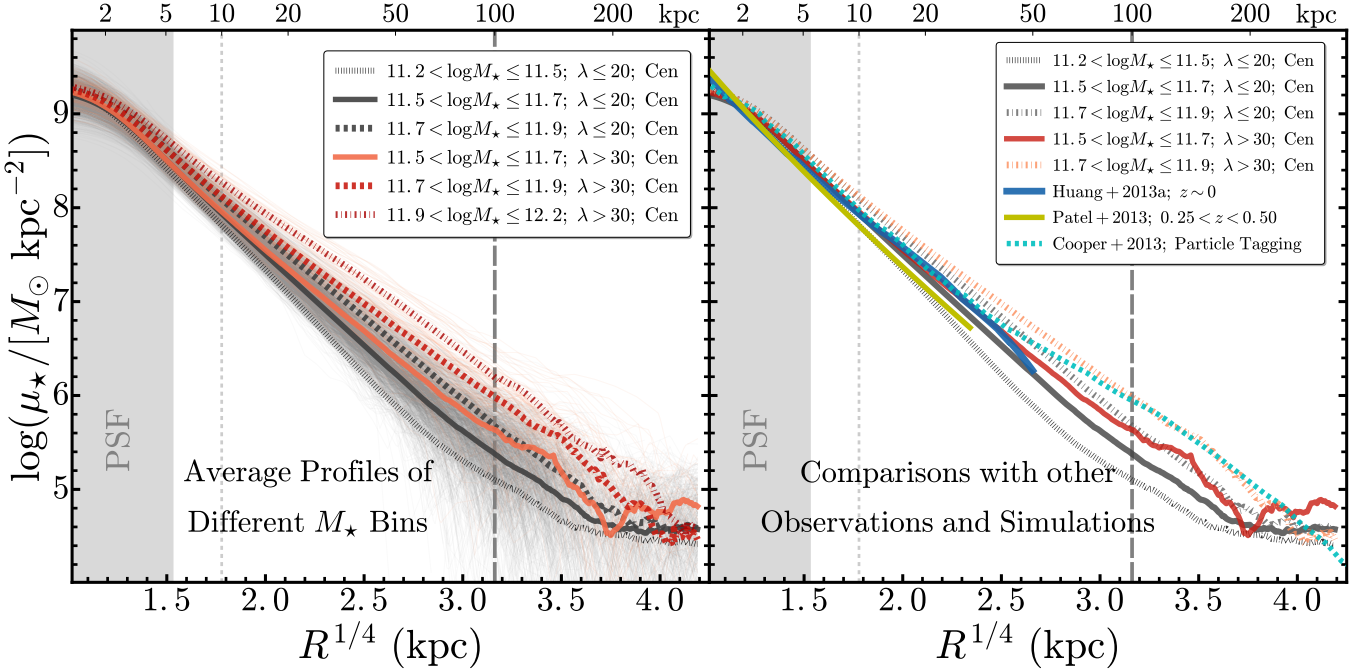


FIG. 5.— Left: stellar mass density (μ_*) profiles of cenHighMh (orange to red) and cenLowMh (grey to black) samples. The radius is in unit of $\text{kpc}^{1/4}$. We show the μ_* profile of individual galaxy in the background using very thin line and light color to highlight the overall distributions of μ_* at different radius. And, we show the average profiles for different M_* bins in much thicker lines. For cenHighMh sample, we separate them into $\log(M_*/M_\odot)$ bins of [11.5, 11.7] (solid line), [11.7, 11.9] (dash line), and [11.9, 12.2] (dot-dash line). As for cenLowMh galaxies, they are grouped into $\log(M_*/M_\odot)$ bins of [11.2, 11.5] (dot-dash line), [11.5, 11.7] (solid line), and [11.7, 11.9] (dash line). We highlight the region that could be affected by seeing using grey shaded region. And, two vertical lines highlight the radius of 10 kpc (thin, dotted line) and 100 kpc (thick, dash line). Right: comparison between the average μ_* profiles with the ones from previous observations and simulations, including: 1) average profile of massive elliptical galaxies at $z \sim 0$ from Huang et al. (2013b, Blue solid line); 2) average profile of massive galaxies at $0.25 \leq z < 0.50$ observed by *HST* from Patel et al. (2013, Yellow solid line); 3) average radial stellar distributions in massive halos using simulation and particle tagging method (Cooper et al. 2013; Cyan dash line). Other formats are the same with the left panel.

out to a few times of the effective radius (color gradient at the very outskirt is still not well quantified). And, for the comparison between the cenHighMh and cenLowMh samples, Our results should remain intact as long as there is no significant differences of color gradient between these two samples. We will discuss this more later, but initial results do suggest a smooth color gradient out to very large radius, and there is no systematic difference in color gradients of the two samples.

Both suggest that the average M_*/L_* approach should work reasonably well for our goals.

And, we should mention that our approach is in principle very similar to the one adopted by the GAMA survey (Taylor et al. 2011), where they start with M_* estimated using average M_*/L_* from SED fitting results of PSF-matched aperture photometry, and later correct it with better estimate of total luminosity. However, the GAMA survey relied on multi-band

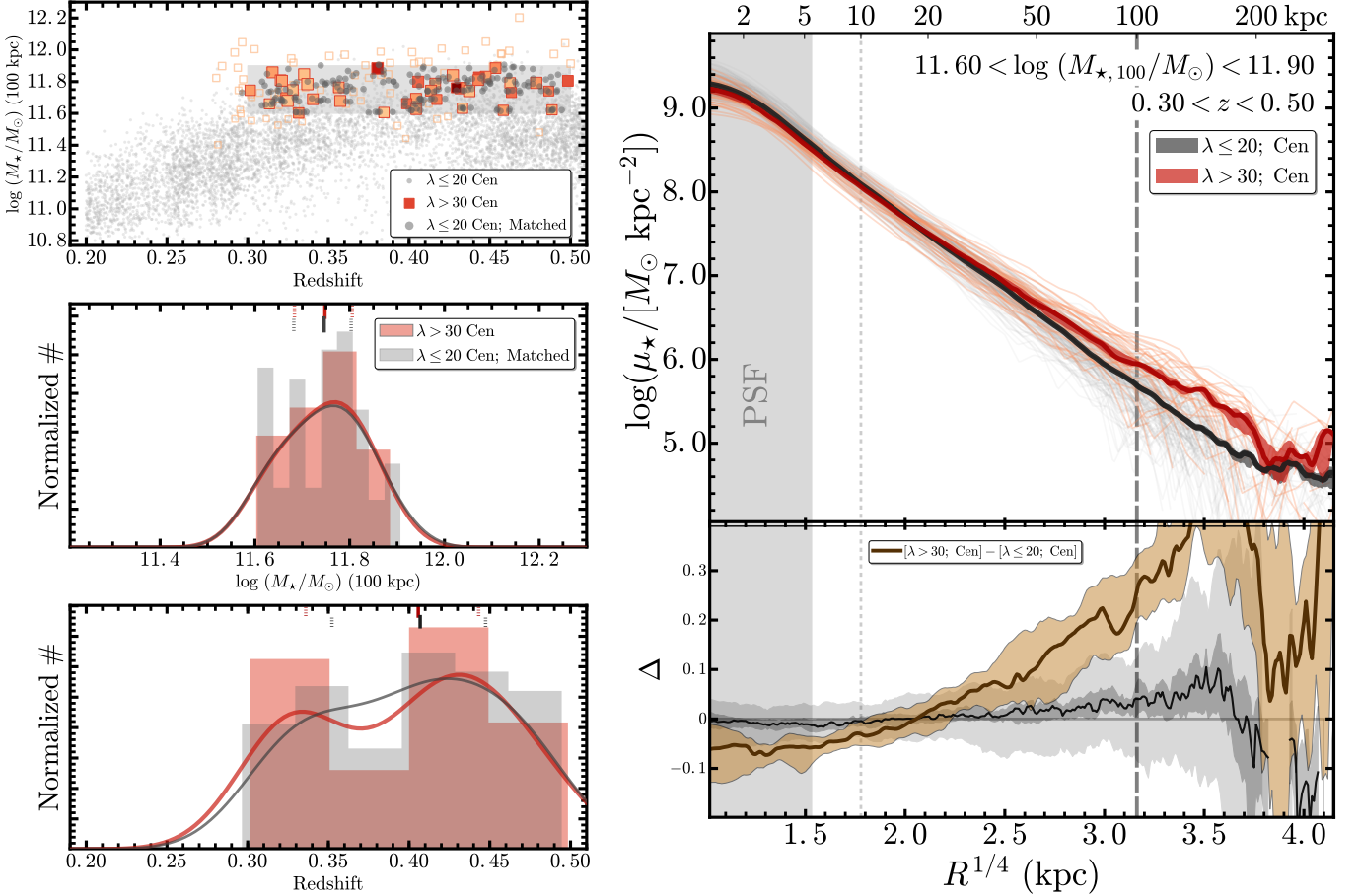


FIG. 6.— Comparison of the μ_* profiles for $M_{*,100\text{kpc}}$ -matched samples of `cenHighMh` (orange to red) and `cenLowMh` (grey to black) galaxies within $11.6 < \log(M_*/M_\odot) < 11.9$. **Left figure** shows the details of the $M_{*,100\text{kpc}}$ -matching process. On the top panel, we show the overall distributions of `cenHighMh` (light orange boxes) and `cenLowMh` (light grey dots) galaxies on the $M_{*,100\text{kpc}}-z$ plane. And, we match the two sample in the $M_{*,100\text{kpc}}-z$ space outlined by the shaded region. We highlight the `cenHighMh` galaxies in this region using bigger boxes in red frames, whose size reflects the P_{Cen} value. We also color-code them using the richness (λ) of the host cluster. The matched `cenLowMh` galaxies are highlighted using darker color and bigger dots. To further evaluate the matching results, we show the distributions of $M_{*,100\text{kpc}}$ (middle panel) and redshift (bottom panel) separately. On both panels, we show the histograms along with their kernel density distributions. And, on the top of each panel, two sets of short vertical lines highlight the median value (solid) and the inter-quartile (dash) of each distribution. **The figure on the right** shows the results of the profile comparison. On its upper panel, we show the μ_* profile of each galaxy using very light color in the background. We highlight the median profile and its corresponding uncertainties using thick solid line with darker color and shaded region. Other formats are the same with Fig. 5. Meanwhile, we highlight the difference between the median profiles and its uncertainty on the bottom panel (brown solid line and shaded region). To test the significance of the differential profile, we perform statistical tests by comparing the median profiles of two random groups that are drawn from the mixed sample, and have the same sizes with the matched `cenHighMh` and `cenLowMh` ones. Repeating this process many times, the median random differential profile (black solid line), their $1-\sigma$ (dark-grey shaded region) and $3-\sigma$ (light-grey shaded region) are highlighted.

single-Sérsic model fitting on the SDSS images to get total luminosity (Kelvin et al. 2012). It is therefore interesting to compare the M_* ($M_{*,\text{GAMA}}$ v.s. $M_{*,100\text{kpc}}$) estimates for galaxies in common, given the differences in data and method. Please see the Appendix C for more details. In short, we notice systematic differences between the two M_* estimates, and it is likely that the GAMA models miss fluxes in the stellar halo that is beyond the depth of SDSS image.

In the left figure of Fig. 4, we show the $M_{*,100\text{kpc}}$ -color relations using the k -corrected $g-r$ color for the `cenHighMh` and `cenLowMh` samples. Both samples follow the same tight red-sequence with very little contamination from star-forming galaxy in the “blue cloud”. And, at fixed $M_{*,100\text{kpc}}$, we see little offset in color distributions of the two samples suggesting that both samples consist of old quiescent galaxies with similar average stellar population properties. This is consistent with previous result that suggests the average stellar population of massive central galaxy does not depend on M_{halo} (e.g. Park et al. 2007). To look into the potential environmental dependence of structure, we will fo-

cus on the mass range of $11.6 \leq \log(M_{*,100\text{kpc}}/M_\odot) \leq 11.9$, where both samples have acceptable completeness, and their $M_{*,100\text{kpc}}$ distributions greatly overlap (see the normalized distributions of $M_{*,100\text{kpc}}$ in the middle panel of Fig. 4). Due to the different sources of redshift for the `cenHighMh` and `cenLowMh` samples, the two samples have quite different redshift distributions (right figure of Fig. 4). Even within the $11.6 \leq \log(M_{*,100\text{kpc}}/M_\odot) \leq 11.9$ mass bin, the redshift differences still differ from each other a little bit. Apparently, the redshift distribution of the `cenLowMh` sample skews toward higher- z end, primarily due to the contribution of BOSS spec-z. This could lead bias into the comparison of μ_* profiles and other properties between the two sample (please see Appendix D for more details). We will address this via matching the two samples in $M_{*,100\text{kpc}}$ and redshift distributions carefully before the comparisons.

5. RESULTS

5.1. Comparison of Surface Mass Density Profiles

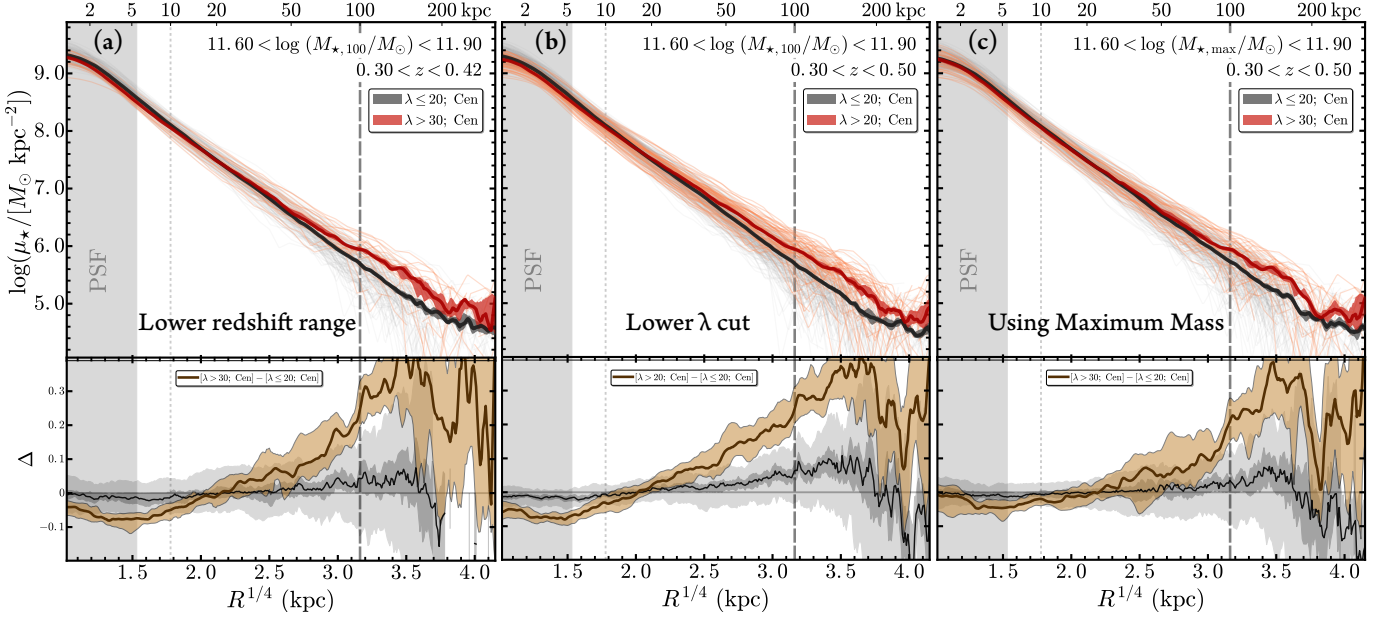


FIG. 7.— Comparisons of the μ_* profiles for cenHighMh (orange-red) and cenLowMh (grey-black) galaxies that are matched using proxies of total M_* . The formats are in consistent with the right figure of Fig.6. The differences are, here, the samples are matched in slightly different ways. From left to right: a) using samples at lower redshift ($0.3 < z < 0.4$); b) using cenHighMh sample with $\lambda > 20$ instead of 30; c) using M_* within 150 kpc instead of 100 kpc. The results are broadly consistent with the one in Fig.6. [Song: Considering to move to a new Appendix.]

5.1.1. Internal Comparison and Comparison with Previous Works

As discussed earlier, although the mass-size scaling relation has been intensely discussed related to the topic of environmental dependence of structure, it may not be the best tool to investigate this problem. Compared to the simple scaling relation, t2he detailed stellar mass density profiles contain much richer structural details that can help us diagnose the role played by different physical processes, including the environmental effect.

Before the actual comparisons, we first show the general properties of these 1-D profiles by separating both samples into different bins of $M_{*,100\text{kpc}}$ and redshift, also by comparing them with results from literature (Fig.5). For profiles in each bin, we derive the median profile along with its uncertainty using bootstrap resampling method (5000 times). The left panel of Fig.5 focuses on different mass bins. As expected, for both samples, higher $M_{*,100\text{kpc}}$ moves the median mass density profile upward a little in the inner region, but makes it more extended in the outer part. In the mass range we explored ($\geq 10^{11.2} M_\odot$), most of these ETGs are slow-rotating (e.g. Cappellari et al. 2013) giant ellipticals with boxy inner isophotal shape (e.g. Kormendy et al. 2009), and flattened density profile at the center (e.g. Lauer et al. 2007), but their structure in the outskirt clearly does NOT response to stellar mass increase in a self-similar way.

In principle, this is consistent with result from HST observations of BCGs at $0.3 < z < 0.9$ (Bai et al. 2014) and the claimed positive correlation between luminosity and Sérsic index (e.g. Savorgnan et al. 2013)¹⁰; it is also consistent with the picture that more massive ETGs experienced more recent (minor) mergers.

At the same time, such behaviour should make us very cautious about any indication of “environmental dependence of structure” as it may be degenerate with difference caused by

¹⁰ But it does not mean such high Sérsic index model works well for massive ETGs as they fail at the inner-most region dramatically, and can not explain the radial variation of isophotal shape

stellar mass when the two samples are not perfectly matched in mass. This is exactly what we see in the median profiles of cenHighMh and cenLowMh in the same mass bins. Although the comparison shows that cenHighMh shows much more extended outer envelope than cenLowMh, the very similar profile in the inner ~ 10 kpc reveals that this is dominated by the different mass distributions in two samples.

In the right panel of Fig.5, we compare these median profiles with a few past works. (Huang et al. 2013b), derived the median stellar mass density profile for a small sample of very nearby ellipticals from the Carnegie-Irvine Galaxy Survey (CGS, Ho et al. 2011). Individual profile and total luminosity were derived from three-component 2-D models that describe both very inner and outer luminosity distributions of these galaxies accurately. The average stellar mass of this sample is around $10^{11.3} M_\odot$. Due to the proximity of this sample (< 100 Mpc), the average profile is unaffected by seeing within ~ 1 kpc. Most galaxies of the CGS sample are not in any cluster. The median profile qualitatively agrees with the median profile of cenLowMh in the low mass bin, especially in the inner region. Outside the inner 15 kpc, the CGS median profile shows a slightly more prominent outer envelope. While this could simply reflect the small size of CGS sample (~ 30), interestingly, it is also consistent with the expectation if the mild mass growth from $z \sim 0.4$ mostly happened at the outskirt. The CGS images are already slightly deeper than SDSS images in r -band, however, the median profile can only reach to ~ 50 kpc (with much larger uncertainty compared to this work) for ETGs within ~ 100 Mpc. Such comparison clearly highlights the improvement made by the deep HSC images as individual profile of $z \sim 0.5$ galaxy is reliable out to at least 100 kpc.

At the similar redshift with our sample, we compare with mass density profile extracted from stacked images of massive ETGs at $0.25 < z < 0.50$ using HST/ACS images (Patel et al. 2013). These galaxies are selected at constant cumulative number density, and as progenitors of $z=0$ massive ETGs. The average stellar mass is $\sim 10^{11.2} M_\odot$ according to

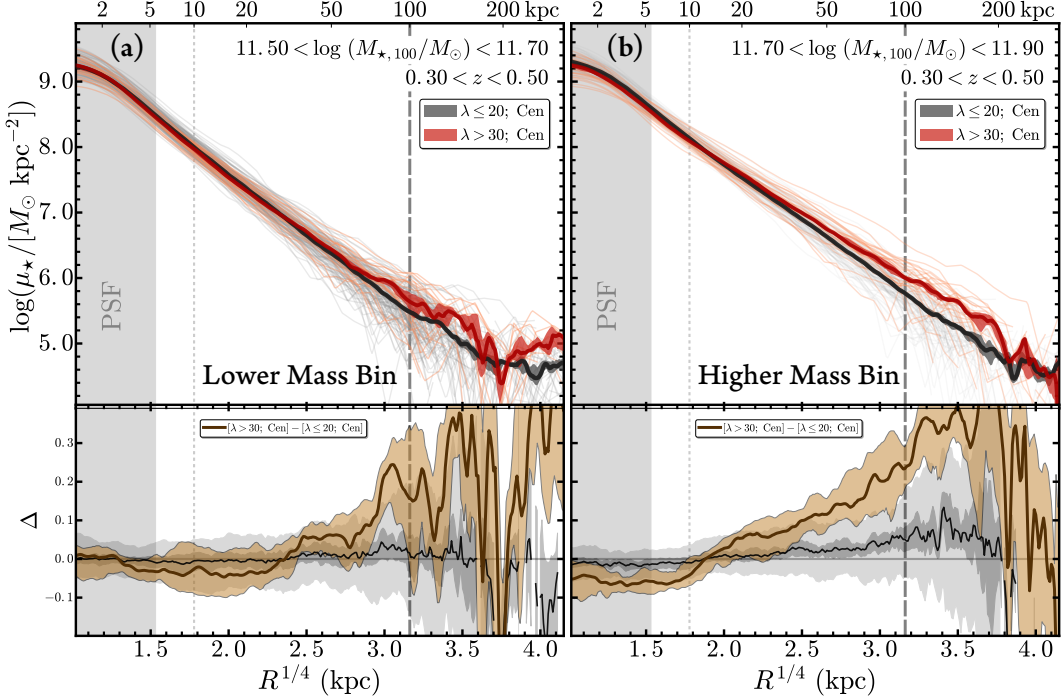


FIG. 8.— Comparisons of the μ_* profiles for `cenHighMh` (orange-red) and `cenLowMh` (grey-black) galaxies in lower (left; [11.5,11.70]) and higher (right; [11.7, 11.9]) $M_{*,100\text{kpc}}$ bins. Other formats are in consistent with the right figure of Fig.6. The difference in median profiles is more significant in higher $M_{*,100\text{kpc}}$ bin.

their estimates. However, given the shallower depth of the ACS images and the usage of the BC03 model (each could cause -0.1 dex mass offset compared to this work), this sample should be comparable to the `cenLowMh` sample in the lowest mass bin, and the comparison of their median profiles does reflect that. Moreover, since the profile from HST/ACS image is not bothered by PSF within 1 Kpc, the comparison illustrates that the HSC median profiles in our redshift range are indeed not affected by seeing outside the shaded region. In fact, as we suggested, our estimate is quite conservative, the profiles within 5 kpc should be reliable.

Besides these observations, we also compare with the predicted average stellar mass density profile for central galaxies of massive halos ($13.5 < \log M_{200,c} < 14.0$) in simulation (Cooper et al. 2013). This is achieved by combining the detailed assembly information of halos from dark-matter-only simulation with semi-analytic model and particle-tagging technique (Cooper et al. 2010). Although the physical resolution and detailed baryonic processes are not as “realistic” as state-of-art hydro-simulation, it is very efficient in providing rough stellar mass distributions for large number of massive halos. Without any adjustment, the profile is quite similar to the `cenLowMh` sample in the $11.5 < \log M_* < 11.7$ bin within inner 20 kpc; but it predicts a too significant outer envelope for its average halo mass. Without going into details to find the cause of such discrepancy in this work, the comparison already suggests that the comparison between deep observed mass density profiles with the ones from modern simulations is going to be quite interesting, especially in the outskirts.

We summarize the median profiles in Fig.5 in Table. 1, and all the above median profiles are available [here](#).

5.1.2. Matched Samples Using $M_{*,100\text{kpc}}$

As stellar mass is considered the most important parameter in determining the structure and other properties of massive

galaxies, it is crucial to make sure the comparison is conducted at “fixed stellar mass”. And, since we directly compare the stellar mass distributions across very large range in radius, it is also important to make sure that differences in physical size of PSF (for more discussion on this issue, please see AppendixC) and imaging depth do not affect the result. In practice, we achieve these by matching the `cenHighMh` and `cenLowMh` samples in the distributions of M_* and redshift in the mass range where both samples have decent completeness. Since the `cenHighMh` sample is much smaller in size, we match the `cenLowMh` sample to it by searching for the N nearest neighbours on the M_* -redshift plane using the KDTree algorithm provided by scikit-learn Python library (Pedregosa et al. 2011). The quality of the matched sample is evaluated by not just the median values of stellar mass and redshift, but also the kernel density distributions (KDE) of these two properties. For M_* , we use a Gaussian kernel with width equals to the typical uncertainty of the mass estimate (0.06-0.10); and for redshift, we choose 0.025 as the width of the Gaussian kernel. As we only keep unique `cenLowMh` galaxies in the matched sample, we manually adjust the value of N to achieve the most similar distribution. In case that the distribution of stellar mass or redshift for `cenHighMh` is bi-modal, we also try to split the sample into two, and match them separately. Normally N is between 3 to 8.

M_* within different radius traces different physical processes and different epochs in the assembly history. In this section, we match the two samples using our proxy of “total” stellar mass, which is the M_* within 100 kpc radius. This choice reflects the stellar mass distributions we can safely measure using model-independent approach given the current depth of the image and the accuracy of sky background subtraction. For galaxies at $11.6 \leq \log(M_*/M_\odot) < 11.9$, 100 kpc equals to 5-8 times of their effective radius, hence should enclose most their stellar mass. Also, for a fraction of massive `cenHighMh` galaxies, the intra-group/cluster light

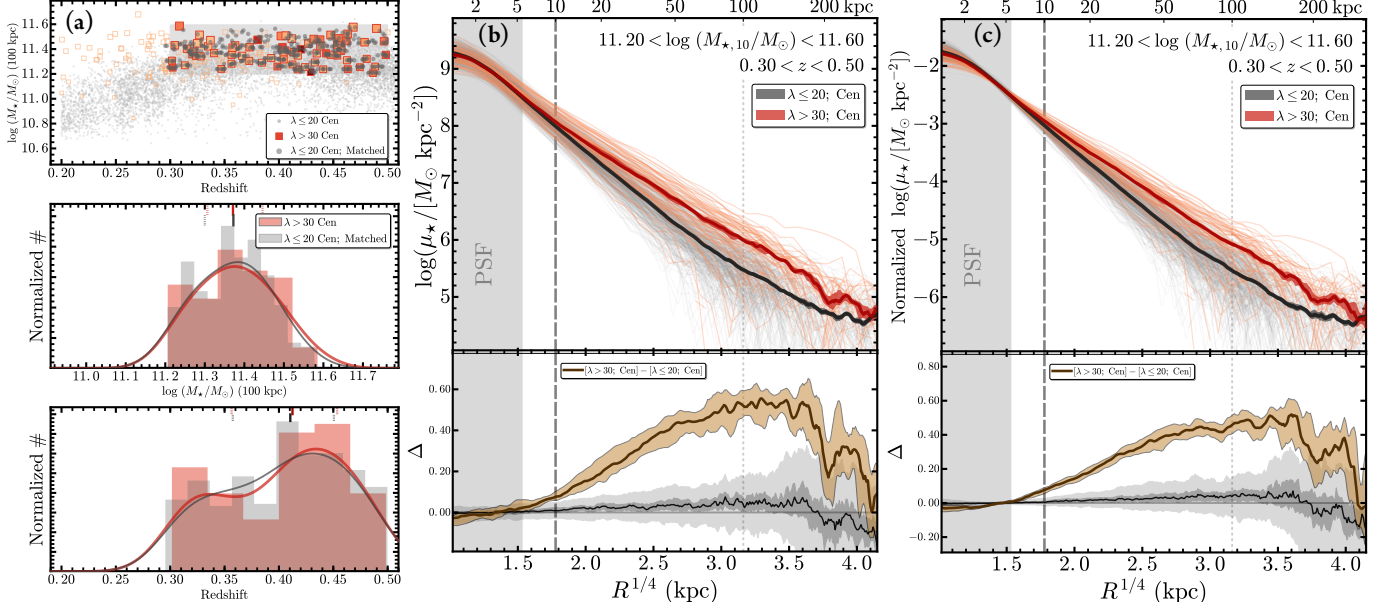


FIG. 9.— Comparisons of μ_* profiles of cenHighMh (orange-red) and cenLowMh (grey-black) samples that are matched using $M_{*,10\text{kpc}}$ instead of $M_{*,100\text{kpc}}$. We perform the match at $11.2 < \log(M_{*,10\text{kpc}}/M_\odot) < 11.6$. **Left figure** shows the matching results in the same format with the left figure of Fig.6. The only difference is $M_{*,100\text{kpc}}$ is replaced by $M_{*,10\text{kpc}}$. **Middle figure** summarizes the profile comparisons in the same format with the right figure of Fig.6. **Right figure** is very similar to the middle one, except we show the profiles that are normalized using the $M_{*,10\text{kpc}}$ value to highlight the scatters of μ_* at different radius. [Song: Have not decided which version to show, or show both like right now; the normal μ_* profile is more objective; but the normalized one highlights both the difference and scatter.]

(IGL/ICL) could dominate their mass profiles outside 100 kpc (**REF**), and complicate the comparison with the cenLowMh galaxies. We will discuss these issues later in Section 6, but in conclusion, the proxy of total M_* and the potential ICL component should not affect the results.

We show the results of the comparison in Fig.6. The left panel highlights the properties of the matched cenHighMh and cenLowMh samples. Given the typical uncertainty of stellar mass, the two samples are well matched in $M_{*,100\text{kpc}}$; and their redshift distributions are broadly consistent with each other. We also check their distributions of k -corrected colors ($g-r$), and confirm that they have very similar average color distributions as well. For the 45 cenHighMh galaxies, we have 229 unique cenLowMh galaxies in the matched sample. On the right side, we plot the individual stellar mass density (μ_*) profile of cenHighMh and cenLowMh galaxies along with the median profiles of both samples. The uncertainties of the median profiles are derived using 5000 times of bootstrap resampling. As one can see, we can comfortably trace the M_* distribution of these massive galaxies out to 100 kpc at individual level, which gives us huge advantage in studying the statistical properties of their outer envelopes. Mass profile out to such large radius was only available for large sample of massive galaxies through image stacking method (**REF**) which suffers from certain systematic issues. Although the μ_* profiles of many galaxies extend well beyond the 100 kpc radius, we notice that some profiles show sign of unphysical truncation that is caused by inaccurate background subtraction. Therefore, we will not include profiles outside 100 kpc in the comparison, even though the median profiles within 200 kpc still behave normally.

Once we match the distributions of $M_{*,100\text{kpc}}$, the μ_* profiles of massive galaxies in the cenHighMh and cenLowMh samples **greatly overlap with each other over the entire radius range**. At fixed “total” stellar mass, massive central galaxies of more massive halos do not form a unique population

comparing to the ones from less massive halos in term of the stellar mass distributions.

At the same time, thanks to the high quality individual profile from HSC image, we can also spot interesting differences in the median profiles of the $M_{*,100\text{kpc}}$ matched cenHighMh and cenLowMh samples. In details, it seems that central galaxy in more massive halos tends to have a slightly flattened inner density profile and possess more significant outer envelope. To highlight such subtle structural features, we show the difference between the two median profiles and its uncertainty in the bottom panel. Given the noticeable uncertainties of $M_{*,100\text{kpc}}$ and λ , and the current small sample sizes, we also perform statistical test to confirm the robustness of the result: we mix the N_r cenHighMh galaxies and the N_n cenLowMh ones together, then randomly draw N_r galaxies with putting-back, compute the difference between the median profile of this sample and the cenLowMh sample, and repeat this process 2000 times. Comparing with the statistical distributions of the differential profiles from this test (grey shaded region), we can now conclude that the structural differences between cenHighMh and cenLowMh samples are much more significant than any statistical fluctuation given the current samples. And, apparently, the “transition radius” where the median profiles of cenHighMh and cenLowMh sample have the same μ_* is $\sim 15\text{-}20$ kpc, which is quite close to the expected R_e of ETGs at this stellar mass.

To further test the robustness of this interesting result, we repeat above procedures to samples with slightly different definition. The results are shown in Fig.7: (a). At higher redshift, the profile is more affected by the seeing at inner region, and by the imaging depth in the outskirt. Therefore, in the left panel, we compare the cenHighMh and cenLowMh samples at $0.3 \leq z < 0.4$, and the results are very similar. (b). We also make the comparison using a cenHighMh sample with lower average halo mass ($\lambda \geq 20$), the results are still stable (middle panel). We also check whether the structural differences

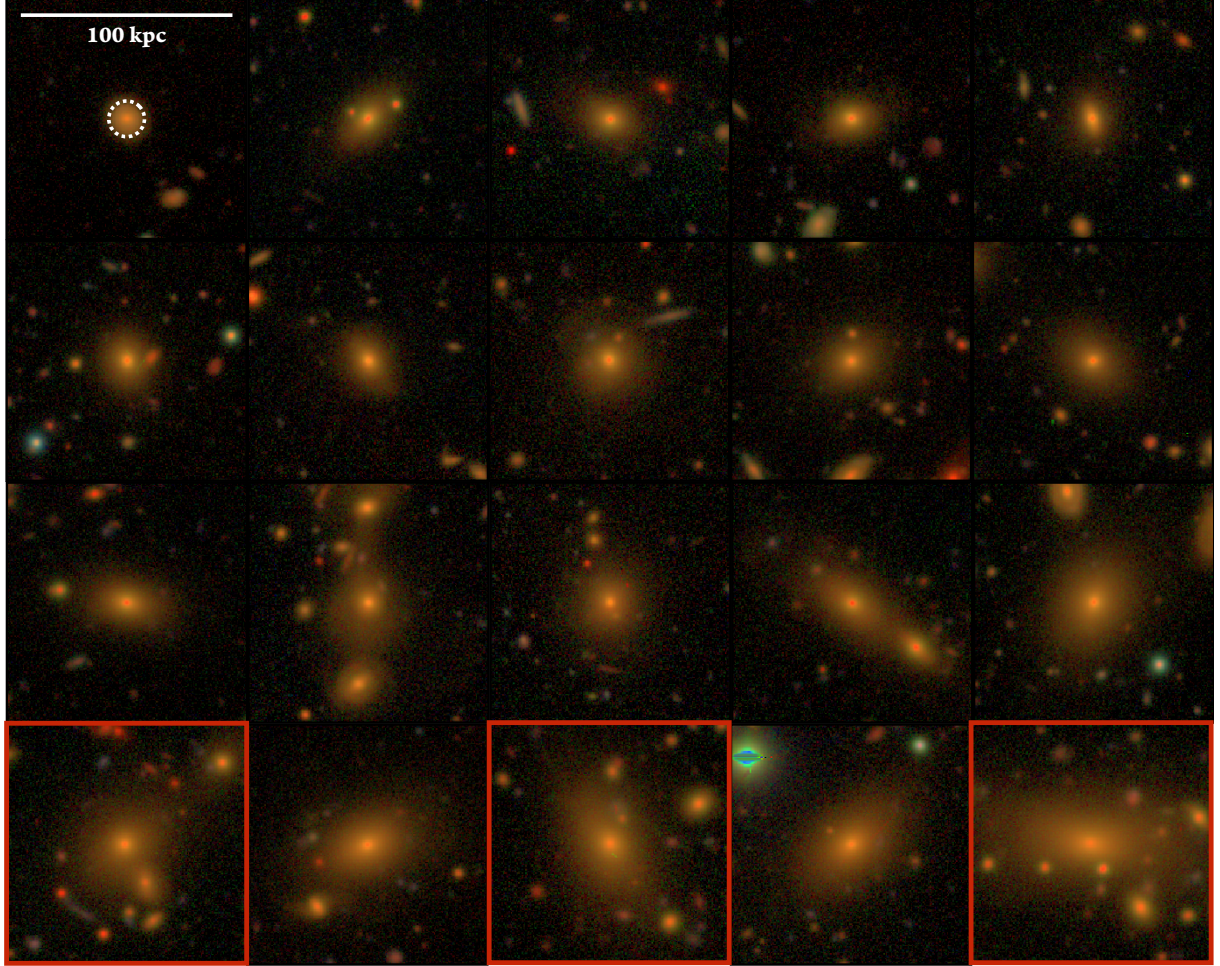


FIG. 10.— Three-color images for a subsample of massive galaxies at similar redshift (~ 0.4), and with similar M_* inside inner 10 kpc (indicated by the dash-line circle on top-left figure; $11.2 < \log(M_{*,10 \text{ kpc}}/M_\odot) < 11.3$). However, they span quite a large range in M_* within 100 kpc (highlighted by the solid bar on the top-left figure). From top-left to bottom-right, their $M_{*,100 \text{ kpc}}$ increases from $10^{11.2} M_\odot$ to $10^{11.7} M_\odot$. The three galaxies from cenHighMh sample are highlighted via red frames.

are driven by small fraction of cenHighMh galaxies in very massive clusters. After removing the cenHighMh galaxies in clusters with $\lambda \geq 40$, the differences are as significant as above. (c). As noted before, the $M_{*,100 \text{ kpc}}$ is just a proxy of the total stellar mass. Given the differences we find, at fixed $M_{*,100 \text{ kpc}}$, cenHighMh galaxy tends to have more prominent outer envelope outside 100 kpc than the cenLowMh one. Hence their real “total” stellar mass could also be slightly larger, and result in bias in the comparison. In the right panel, we make the comparison using the maximum stellar mass from the integration of the μ_* profile instead of the $M_{*,100 \text{ kpc}}$. In this case, the differences between the median profiles become slightly less significant as expected. But the systematic trends, especially the differences in the low mass density outskirt are still very stable. All these tests confirm that we robustly detect subtle, but systematic structural dependence on halo mass of massive galaxies. The fact that it requires such careful comparison to reliably reveal any potential halo mass dependence already suggests that the role environment played in shaping these massive galaxies is not crucially important. At the same time, the systematic differences we find, especially the more extended stellar envelope of massive central galaxy in more massive halos, seem to be consistent with the expectation of richer (minor) merging history in denser environment. We will discuss these more in Section 6.

We also explore the possible $M_{*,100 \text{ kpc}}$ dependence of such difference. Limited by the small sample we have, we can only afford to separate the samples into two $M_{*,100 \text{ kpc}}$ bins ($11.5 \leq \log(M_{*, 10 \text{ kpc}}/M_\odot) < 11.7$ and $11.7 \leq \log(M_{*, 10 \text{ kpc}}/M_\odot) < 11.9$). After performing the same procedures of sample matching and comparison, we show the results in Fig. 8. Although the smaller sample leads to larger statistical uncertainties, it is still interesting to see that the structural differences seem to be more significant in the higher $M_{*,100 \text{ kpc}}$ bin. For the lower $M_{*,100 \text{ kpc}}$ bin, the difference in the inner region becomes quite uncertain, while there is still evidence that suggest difference in the outskirt. This result also has interesting implications in studying the assembly of massive galaxies, and is worth further investigation with larger sample in the future.

5.1.3. Matched Samples Using $M_{*,10 \text{ kpc}}$

As suggested by the popular two-phase formation scenario of massive galaxies, the inner 5-10 kpc of these galaxies (within $0.5-1xR_e$) is dominated by stars formed in intensive dissipative processes at high redshift, and is less affected by the succeeding merging events. This picture is broadly supported by the redshift evolution of μ_* profile of massive galaxies (REF), structure decomposition of nearby massive galaxies (REF), and their radial distributions of stellar population (REF). Certainly, major merger can induce violent relaxation

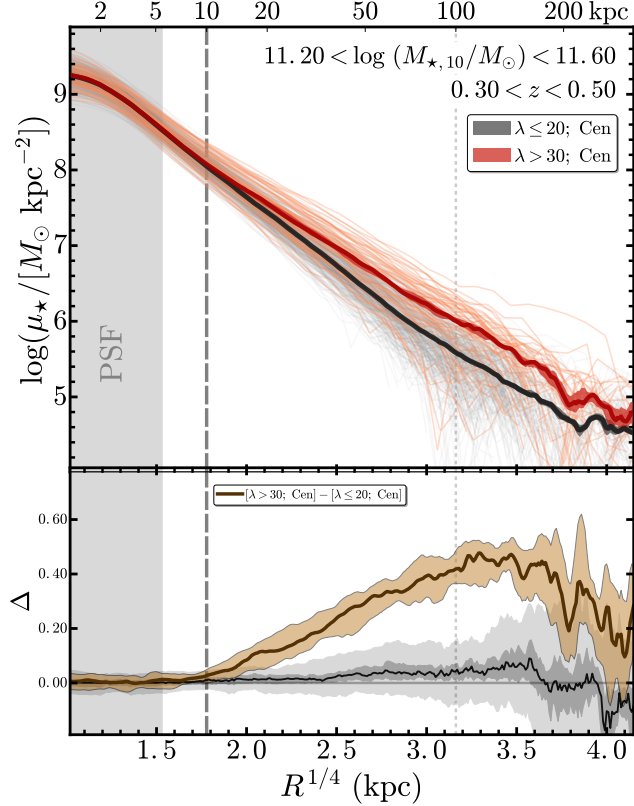


FIG. 11.— Comparisons of unnormalized μ_* profiles of $\log(M_{*,100}/M_\odot) > 11.5$ cenHighMh (orange-red) and cenLowMh (grey-black) samples that are matched using $M_{*,10\text{kpc}}$. Except for the difference in $M_{*,100\text{kpc}}$ -limit of both samples, other formats are the same with the middle figure of Fig.9. [Song: The reason I did this test is because the $M_{*,10\text{kpc}}$ matched cenLowMh sample without any constraint will have a lot of galaxies with $M_{*,100\text{kpc}} < 10^{11.5} M_\odot$ in the sample; They are in the $M_{*,100\text{kpc}}$ -incomplete range, and it is harder to argue that they have similar mass in the ‘in-situ’ component with the cenHighMh ones. If you think this is weird, another choice is to do the match at $M_{*,10\text{kpc}}$ in between [11.4, 11.6], so that most galaxies have $M_{*,100\text{kpc}} > 10^{11.5} M_\odot$.]

process that modifies the stellar mass distribution even in the central region, and must happen to these massive galaxies in last 6-8 Gyrs, it may not invalidate the above assumption. For galaxy this massive, the last major merger event is highly likely to be non-dissipative, and the redistribution of stars is basically according to their binding energy in the host halo. The inner region of the final merger remnant is still mostly composed of the “in-situ” stars from the two progenitors.

Therefore, it is interesting to compare the cenHighMh and cenLowMh samples that are matched using mass within the inner region. In this work, we choose to use the mass within inner 10 kpc ($M_{*,10\text{kpc}}$). As we can see in previous profile comparison, $M_{*,10\text{kpc}}$ is not affected by the physical size of PSF out to $z = 0.5$. We use the same procedure to match the cenLowMh galaxies to the cenHighMh ones using $M_{*,10\text{kpc}}$ (within $11.2 \leq \log(M_{*, 10\text{kpc}}/M_\odot) < 11.6$) and redshift ($0.3 \leq z < 0.5$). For the 56 galaxies in this cenHighMh sample, we achieve excellent matching result using 375 cenLowMh galaxies (see Fig.9). Using the same method, we show their individual profiles, and the comparison of their median μ_* profiles in Fig.9. Unlike the $M_{*,100\text{kpc}}$ matched samples, here we see very striking differences that are already very significant even without any statistical test. As we can see, when matched using $M_{*,10\text{kpc}}$, the μ_* profiles of cenHighMh and cenLowMh galaxies have quite similar μ_* profiles in the inner

5-10 kpc, in great contrast of the differences at outer region where the cenHighMh galaxies show much more extended envelope. Besides the difference in the median profiles, it is also worth discussing the distributions of individual μ_* profiles. Combining the cenHighMh and cenLowMh samples together, it is easy to notice that the dynamical range of μ_* at fixed radius is much larger in the outskirt. This becomes even more clear when we further normalize each profile using the $M_{*,10\text{kpc}}$ value (see Fig.9). For both cenHighMh and cenLowMh samples, we find that their outer μ_* profiles clearly show much larger diversity comparing to the inner region.

Putting together, these results indicate that massive central galaxies with similar $M_{*,10\text{kpc}}$ and inner mass profiles can span a huge range in total stellar mass, and can have very different mass distributions in the outskirt. We further highlight this by showing the 3-color images of randomly selected massive central galaxies (see Fig.10) that have similar $M_{*,10\text{kpc}}$ ($11.1 \leq \log(M_{*, 10\text{kpc}}/M_\odot) < 11.2$) but different $M_{*,100\text{kpc}}$. From the top-left to the bottom-right, the $M_{*,100\text{kpc}}$ of these galaxies increases from $10^{11.22} M_\odot$ to $10^{11.75} M_\odot$.

Since the two samples are matched using $M_{*,10\text{kpc}}$, the cenLowMh sample starts to include galaxies with $11.2 \leq \log(M_{*, 100\text{kpc}}/M_\odot) < 11.6$. On one hand, they are likely to be the central galaxies in halos that are much smaller than the ones in cenLowMh sample, which still mostly consists of galaxies with $\log(M_{*, 100\text{kpc}}/M_\odot) \geq 11.6$. Hence, above results may hint that the outer μ_* profile of central galaxy could have a clear dependence on the halo mass. This is a very interesting clue that deserves more investigations including comparison with simulations. But, on the other hand, we need to recognize that the mass completeness of our current cenLowMh sample is still not satisfying; and in this lower $M_{*,100\text{kpc}}$ range, small fraction of satellite contamination should be expected even though we already excluded satellites in known cluster using the redMaPPer catalog. To naively test the robustness of these results, we match the two samples using $M_{*,10\text{kpc}}$ again, but only include galaxies with $\log(M_{*, 100\text{kpc}}/M_\odot) \geq 11.5$. Comparison between these two more complete, purer samples of massive central galaxies at fixed $M_{*,10\text{kpc}}$ reveals very similar behavior¹¹ (see Fig.11), supporting the robustness of the results. And, we also try to match the two samples using mass within 5 and 15 kpc instead, the results are also very similar.

5.2. Explore Different Scaling Relations

5.2.1. M_* -size relation

The scaling relation between M_* and effective radius (or half-light radius) was the focus of past investigations of the structural evolution (e.g. REF) and the environmental dependence of structures for massive galaxies (e.g. REF). So far, the results are quite confusing as no clear evidence of environmental dependence has been found at low redshift using various definitions of “size”. Also, at high redshift, the results can be even controversial (e.g. REF). As the deep HSC images have already help us reveal subtle, but systematic structural differences in massive central galaxies that may depend on the environment, we should expect to see such evidence on the mass-size relation. Here, we briefly discuss the mass-size relations of cenHighMh and cenLowMh galaxies (Fig.12).

¹¹ In fact, their median profiles become even more similar in the inner region

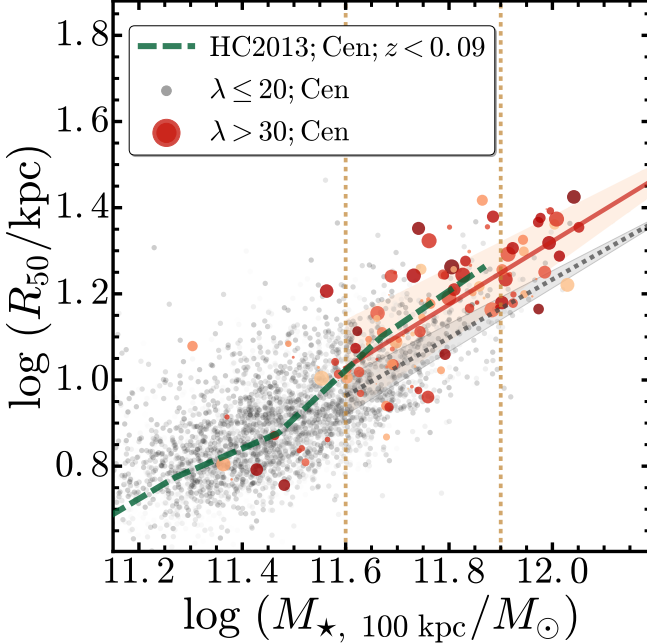


FIG. 12.— The M_* -size relations for cenHighMh (orange-red circles) and cenLowMh (grey dots) galaxies. Here we use the $M_{*,100\text{kpc}}$ as proxy of “total” M_* , and use the R_{50} derived from the 1-D profile as size estimate. The size and color coding for cenHighMh galaxies are the same with the right panel of Fig.3. And two vertical lines highlight the $11.6 < \log(M_*/M_\odot) < 11.9$ mass range. We also compare these distributions with the relation for nearby central galaxies of massive groups from Huertas-Company et al. (2013) (green, long dashed line). The M_* and R_e are estimated via different methods in these works. We also illustrate best-fit M_* - R_{50} relations for cenHighMh (red, solid line) and cenLowMh (grey, dash line) galaxies that have $\log(M_{*,100\text{kpc}}/M_\odot) \geq 11.6$. The shaded regions in lighter color show the $1-\sigma$ uncertainties of these relations. Please refer to the text for detailed comparisons.

We choose to use the $M_{*,100\text{kpc}}$ as the proxy of “total” M_* , and use the half-light radius (R_{50}) that is defined as the radius enclosing 50% of luminosity within 100 kpc as the “size” to evaluate the relation. And, we use the curve-of-growth of luminosity from the Ellipse run on i -band images to estimate the R_{50} here. In principle, such approach is more sensitive to issues like the smearing effect of PSF and the choice of aperture for maximum luminosity than the 2-D fitting method. For the massive galaxies in this work, their apparent sizes are always sufficiently large at $0.3 \geq z \geq 0.5$ so that the R_{50} measurement is not bothered by PSF. And, the 1-D method has the advantages of being less affected by accuracy of background subtraction, structural details, and model assumptions.

We show the distributions of cenHighMh and cenLowMh galaxies on the mass-size plane. On top of the clear correlations for both sample, the distributions of R_{50} for cenHighMh and cenLowMh samples greatly overlap with each other over the $M_{*,100\text{kpc}}$ range between $10^{11.6}$ and $10^{11.9} M_\odot$. Meanwhile, it seems that the cenHighMh galaxies do have a slightly higher R_{50} . For the $M_{*,100\text{kpc}}$ matched samples used in Fig.6, the median $\log(R_{50}/\text{kpc})$ values for the cenHighMh and cenLowMh are 1.22 ± 0.02 ($\sim 17.4 \pm 0.75$ kpc) and 1.09 ± 0.01 ($\sim 12.3 \pm 0.3$ kpc), which confirm the above observation and is consistent with the differences seen in Fig.6. However, all previous works that we are aware of did not match the mass (and redshift) distributions between different samples, and often focus on the form of the $\log(M_*/M_\odot)$ - $\log R_e$ relation. Here, we try to derive the best-fit parameters for the $\log(M_{*,100\text{kpc}}/M_\odot)$ - $\log(R_{50}/\text{kpc})$ relations of galax-

ies with $\log(M_{*,100\text{kpc}}/M_\odot) \geq 11.6$ using MCMC-sampling method via the ensemble sampler emcee (Foreman-Mackey et al. 2013). Using initial guesses based on maximum likelihood estimates, and assuming reasonable flat priors, we derive best-fit relation for the massive cenHighMh galaxies:

$$\log(R_{50}/\text{kpc}) = (0.73 \pm 0.13) \times \log(M_{*,100\text{kpc}}/M_\odot) - (7.49 \pm 1.56) \quad (1)$$

And for the massive cenLowMh galaxies, we have:

$$\log(R_{50}/\text{kpc}) = (0.68 \pm 0.06) \times \log(M_{*,100\text{kpc}}/M_\odot) - (6.88 \pm 0.75) \quad (2)$$

As shown in Fig.12, at the high-mass end, the two relations have consistent slopes within their uncertainties, but different normalizations. Extending the fitting to the full $\log(M_{*,100\text{kpc}}/M_\odot)$ range does not change this result. We also explore mass-size relations for our samples using M_* within different radius (e.g. 120, 150 kpc) and the R_{50} derived within these apertures, and find consistent results.

We qualitatively compare our results with the one for $z \leq 0.09$ central ETGs in $14 \leq \log(M_{\text{Halo}}/M_\odot) < 15$ halos from Huertas-Company et al. 2013 (HC13; green solid line). HC13 use the group catalog by Yang et al. (2007) to estimate $\log(M_{\text{Halo}}/M_\odot)$. They estimate the 2-D R_e using single-Sérsic model fitting to SDSS images, and derive M_* based on SED fitting using the BC03 (Bruzual & Charlot 2003) synthetic population model. We empirically convert their M_* from the Kroupa IMF to the Chabrier one used in this work by applying a constant -0.03 shift to their values. We also increase the M_* in HC13 by +0.1dex to account for the systematic difference between their BC03 and our FSPS model (see Appendix B). In HC13, the authors found no difference among the mass-size distributions for central galaxies in halos across $12.5 \leq \log(M_{\text{Halo}}/M_\odot) < 15.0$. Despite all the systematic differences, the mass-size distributions for both cenHighMh and cenLowMh galaxies follow the HC13 relation reasonably well (with slightly shallower slopes) even at $\log(M_{*,100\text{kpc}}/M_\odot) < 11.6$ where our samples start to become incomplete.

In short, we confirm that the massive central galaxies in this work generally follow the mass-size relation of massive ETGs at low- z . And, more importantly, we find evidence of differences in the mass-size relations for massive central galaxies of halos with different M_{halo} . The difference we saw at $\log(M_{*,100\text{kpc}}/M_\odot) \geq 11.6$ is in line with the conclusion that central galaxies in denser environment have slightly larger size comparing to the ones from less-dense environment at fixed M_* .

This suggests that the previous, inconclusive results on whether the mass-size relation of massive ETGs depends on environment could be due to either the inadequate depth of the image, or the inappropriate model assumptions adopted during the fitting (or both). It would be interesting to revisit this issue using 2-D models based on deep HSC images as the next step. It is worth noting that our results are based on massive galaxies at $z \sim 0.4$, while the sample of HC13 has $z < 0.09$. Although here we can not address the interesting issue of redshift evolution of mass-size relation, the “evolutionary path” of massive central galaxies from different environments on this mass-size plane is certainly an intriguing issue. If the cenHighMh galaxies have a richer merging history

than the `cenLowMh` ones, perhaps we should expect more significant differences on their mass-size relations and average μ_* profiles at $z \sim 0$ using deeper image. On the other hand, if the `cenLowMh` galaxies could assemble more M_* through minor mergers in the last 3-4 Gyrs, they could “catch-up” with the `cenHighMh` galaxies a little bit on the mass-size plane. Potentially, we could make some predictions on this issue using the frequency of tidal features and properties of satellites around our `cenHighMh` and `cenLowMh` galaxies in the near future.

5.2.2. Relations between stellar mass within different physical apertures

We just show that the mass-size relation of massive central galaxies could also depend on the mass of their host halos, and here we explore relationships between M_* within different apertures as alternative tools to help us better understand the relationship between halo mass and assembly history of massive galaxies. Here we focus on $M_{*,100\text{kpc}}$, $M_{*,10\text{kpc}}$, and also the logarithmic mass differences between them ($\Delta \log M$, reflecting M_* ratio). Comparing to the mass-size relation, such relations are not affected by the ambiguous definition of “size”; and comparing to the detailed μ_* profiles, it is much easier to apply these relations to larger samples and compare with results from simulations.

We show the results in Fig.13. In panel (a), we plot the $M_{*,100\text{kpc}}$ with $\Delta \log M$ for both the `cenHighMh` and `cenLowMh` samples. As expected, these two parameters well trace each other over the entire $M_{*,100\text{kpc}}$ range, indicating that more massive central galaxies have larger fraction of total M_* in the outer part. Suggested in Fig.8, the structural differences related to M_{halo} seem to be more significant in higher M_* bin. We therefore highlight the $M_{*,100\text{kpc}}$ -matched `cenHighMh` and `cenLowMh` galaxies at $11.7 \leq \log(M_{*,100\text{kpc}}/M_\odot) < 11.9$. Although their $\Delta \log M$ distributions still greatly overlap within this $M_{*,100\text{kpc}}$ range, the median values (big, outlined symbols with error bars), and their kernel-density distributions clearly point out systematic difference. Consistent, but slightly smaller, difference also exists for $M_{*,100\text{kpc}}$ -matched samples at $11.6 \leq \log(M_{*,100\text{kpc}}/M_\odot) < 11.9$. At the same time, the comparisons in Fig.6 and Fig.8 also suggest that the $M_{*,100\text{kpc}}$ -matched `cenHighMh` galaxies have lower $M_{*,10\text{kpc}}$ than the `cenLowMh` sample, which is clearly shown by panel (b) where we plot $\Delta \log M$ with $M_{*,10\text{kpc}}$ for the $M_{*,100\text{kpc}}$ -matched samples. For the `cenLowMh` sample, the correlation between $\Delta \log M$ and $M_{*,10\text{kpc}}$ is much weaker than the one in panel (a), yet it is still visible. However, for our `cenHighMh` sample, we see no overall correlation between $\Delta \log M$ and $M_{*,10\text{kpc}}$. We also construct $\Delta \log M$ using logarithmic mass differences between 100 and 30 (or 50) kpc, and the results are very similar. In fact, the average differences between the $M_{*,100\text{kpc}}$ -matched `cenHighMh` and `cenLowMh` samples become more significant when mass within 30 (or 50) kpc is used. These reflect the structural differences we found in Fig.6: at fixed $M_{*,100\text{kpc}}$, central galaxies with higher M_{halo} tend to have even higher fraction of M_* stored between 10 and 100 kpc.

In panel (c), we show the relationship between $\Delta \log M$ and $M_{*,100\text{kpc}}$, and highlight the $M_{*,10\text{kpc}}$ -matched samples presented in Fig.9 and Fig.11. Using the histograms of $M_{*,100\text{kpc}}$ and their median values of the $M_{*,10\text{kpc}}$ -matched samples, we clearly identify the impact from the much more extended outer envelope hosted by `cenHighMh` galaxies.

Finally, in panel (d), we plot $M_{*,100\text{kpc}}$ against $M_{*,10\text{kpc}}$ di-

rectly. The median values and statistical distributions of $M_{*,10\text{kpc}}$ for the $M_{*,100\text{kpc}}$ -matched samples highlight the structural difference at fixed $M_{*,100\text{kpc}}$ again. All the M_{halo} -dependence of structures we discussed above are clearly displayed here along the directions of both x- and y-axis. Firstly, within the $M_{*,100\text{kpc}}$ range we explored, the `cenHighMh` galaxies tend to have lower mass within the inner 10 kpc; and such difference seems to become more significant at higher $M_{*,100\text{kpc}}$. As seen from the median μ_* profiles, this is due to the shallower overall profile of `cenHighMh` galaxy, and indicates that the slopes of both inner and outer μ_* profiles of massive central galaxies may depend on M_{halo} . Secondly, for massive central galaxies that form similar amount of stars through the dissipative processes during the “in-situ” phase (approximated by $M_{*,10\text{kpc}}$), their $M_{*,100\text{kpc}}$ distributions at lower redshift depend on M_{halo} in a way that the ones in more massive halos can develop much more prominent stellar envelope thanks to the more complex mass assembly history.

But, more importantly, it is intriguing to see that the distributions of `cenHighMh` and `cenLowMh` galaxies on this 2-D plane seem to be offset with each other. At least at the high mass end, the central galaxies in more and less massive halos seem to follow relations between $M_{*,100\text{kpc}}$ and $M_{*,10\text{kpc}}$ with similar slopes, but different normalizations. Instead of subjectively grouping galaxies into different bins of $M_{*,100\text{kpc}}$ or $M_{*,10\text{kpc}}$, such scaling relation brings us a more generic view of the environmental dependence of structure, and could become an interesting tool to investigate the connection between halo mass, assembly history, and the structure of massive galaxies. On Fig.13 (d), we illustrate the $\log(M_{*,100\text{kpc}}/M_\odot)$ - $\log(M_{*,10\text{kpc}}/M_\odot)$ relations at $\log(M_{*,100\text{kpc}}/M_\odot) \geq 11.6$ that are derived using MCMC sampling method. For `cenHighMh` galaxies, the best-fit relation is:

$$\log(M_{*,10\text{kpc}}/M_\odot) = (0.48 \pm 0.06) \times \log(M_{*,100\text{kpc}}/M_\odot) + (5.72 \pm 0.75) \quad (3)$$

While for the `cenLowMh` ones within the same $M_{*,100\text{kpc}}$ range, we have:

$$\log(M_{*,10\text{kpc}}/M_\odot) = (0.56 \pm 0.03) \times \log(M_{*,100\text{kpc}}/M_\odot) + (4.82 \pm 0.30) \quad (4)$$

The same relation using the full $M_{*,100\text{kpc}}$ range will result in a even shallower slope for the `cenHighMh` galaxies. And, replacing the $M_{*,10\text{kpc}}$ with M_* within 5 or 15 kpc apertures does not change our conclusion. In fact, the relation using $M_{*,5\text{kpc}}$ shows more significant M_{halo} dependence at the high-mass end. Unfortunately, due to the impact from PSF, the $M_{*,5\text{kpc}}$ values are slightly less reliable than the $M_{*,10\text{kpc}}$ ones. Samples at lower redshift, images from space telescope, and 2-D modeling method can all help us pushing this investigation further insider smaller physical aperture that perhaps can provide us better surrogate of M_* from the “in-situ” phase.

Besides the systematic offset, it seems that the `cenHighMh` galaxies could have larger scatter of $M_{*,10\text{kpc}}$ at high-mass end. Limited by our capability to estimate the mass and other properties of halos at individual level, we can not further quantify this potential M_{halo} -dependence here. Within the `cenHighMh` sample, we do not find any evidence of dependence on the richness (λ) of the cluster even the `redMaPPer` richness should traces M_{halo} reasonably well.

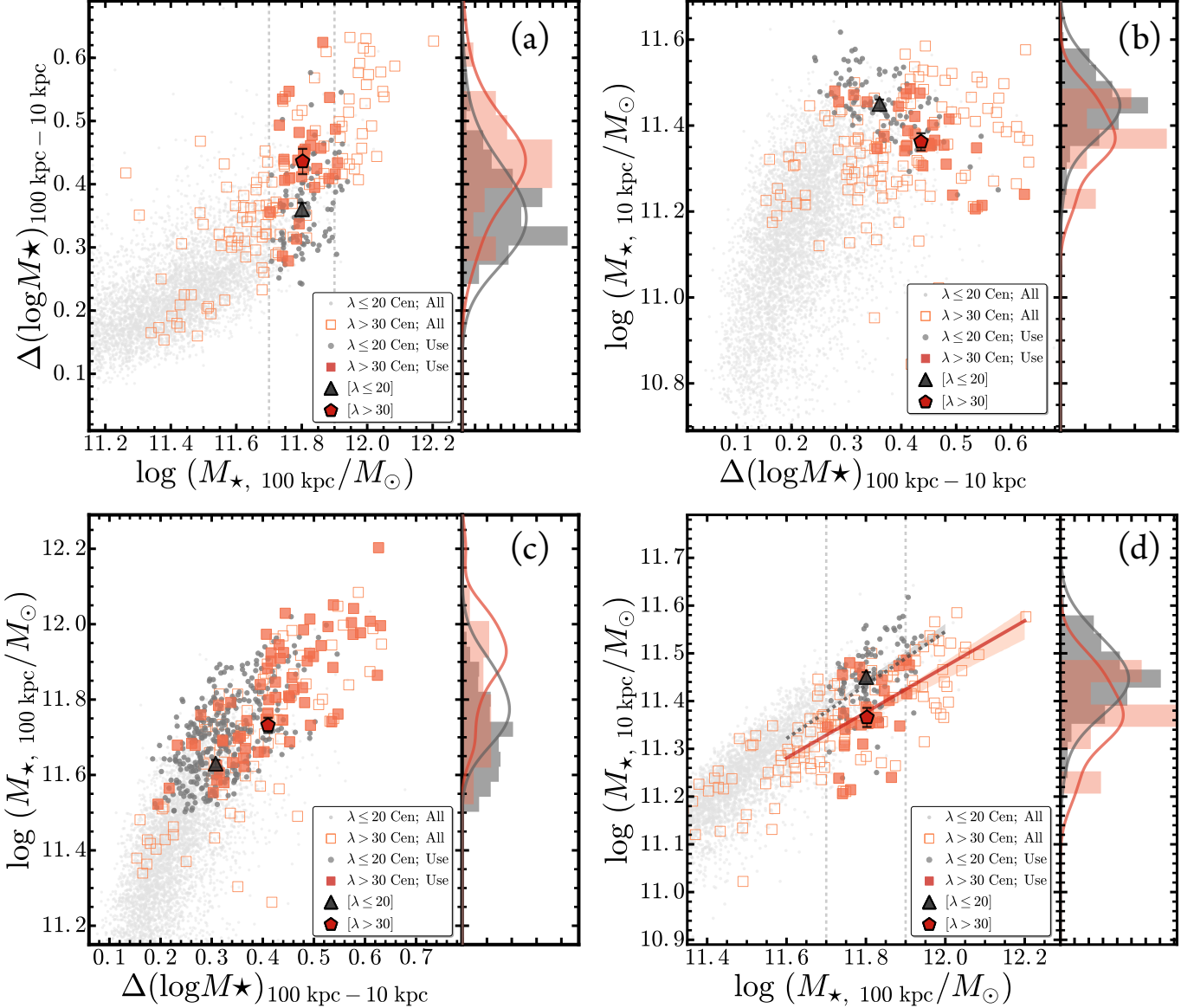


FIG. 13.— (a): Distributions of galaxies on the $M_{\star,100\text{kpc}}-\Delta(\log M_\star)_{100\text{kpc}-10\text{kpc}}$ plane. All cenHighMh (open red boxes) and cenLowMh (light, grey dots) galaxies are shown in the background. The $M_{\star,100\text{kpc}}$ -matched samples between $11.6 < \log(M_\star/M_\odot) < 11.9$ (between two vertical lines) are highlighted (cenHighMh: solid red boxes, color and size coding are the same with right panel of Fig.3; cenLowMh: bigger grey dots). We also show the median values (solid triangular and hexagon), and the distributions of $\Delta(\log M_\star)_{100\text{kpc}-10\text{kpc}}$, both histograms and kernel density distributions on the right. (b): Distributions of galaxies on the $\Delta(\log M_\star)_{100\text{kpc}-10\text{kpc}}-M_{\star,10\text{kpc}}$ plane. (c): Distributions of galaxies on the $\Delta(\log M_\star)_{100\text{kpc}-10\text{kpc}}-M_{\star,100\text{kpc}}$ plane. But, this time, we highlight the cenHighMh and cenLowMh samples that are matched using $M_{\star,10\text{kpc}}$ instead of $M_{\star,100\text{kpc}}$. (d): Relations between $M_{\star,100\text{kpc}}$ and $M_{\star,10\text{kpc}}$. Other formats of figure (b), (c), and (d) are very similar with figure (a).

In the current sample, most of the cenHighMh galaxies are centrals of clusters with $30 \leq \lambda \leq 40$, and only small fraction comes from more massive clusters. Together with the small sample size, the uncertainties of richness from shallow SDSS images, and the intrinsic scatter of the λ - M_{halo} relation may conspire to hide more detailed M_{halo} -dependence.

The evidence of M_{halo} -dependence of structure in massive galaxies could be caused by different processes, it is therefore of great interest for us to dig deeper by comparing the galaxies at higher redshift or from numerical simulations (e.g. see Fig.1 of Wellons et al. 2016) on the $M_{\star,100\text{kpc}}-M_{\star,10\text{kpc}}$ or similar planes.

6. DISCUSSIONS

In the past decade, the mass assembly and structural evolution of massive ETGs remains as an active topic. More and more convincing observations of massive galaxies at high redshift reveal that the progenitors of massive elliptical galaxies are quite different in structure comparing with their local decedents (e.g. REF). Collectively, they need to increase their “size” (R_e) by a factor of 2 to 4 (e.g. REF) without changing their inner μ_\star profile (e.g. REF) and central stellar velocity dispersion (e.g. REF) much in the last 8-10 Gyrs. Owing mainly to better numerical simulations, the challenge of “size”-evolution seems to be eased by the promising “two-phase” scenario under the framework of hierarchical formation of galaxy (e.g.REF). Under this picture, the inner region of massive galaxies mostly consist of stars formed within the halo of the main progenitor through intense dissipative pro-

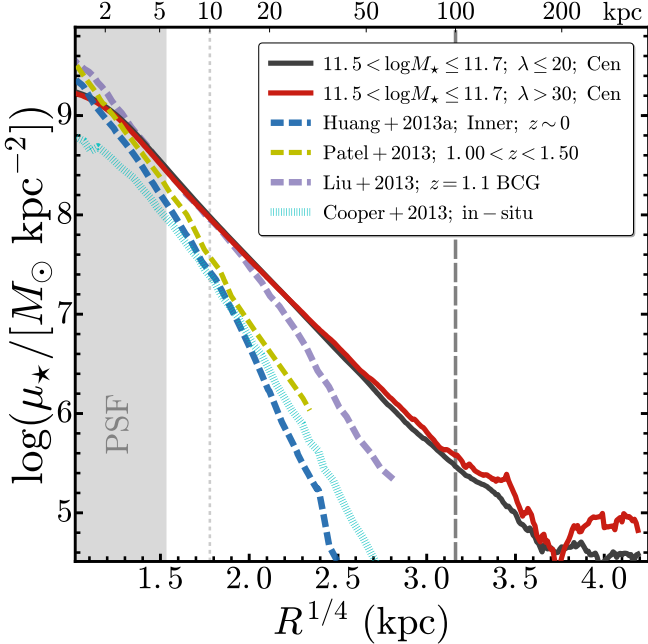


FIG. 14.— Comparison of the average μ_* profiles of both cenHighMh (red) and cenLowMh (black) galaxies at $11.5 < \log(M_*/M_\odot) < 11.7$ with other observations and simulations. The format is very similar with the right panel of Fig.5, except that here we focus on the μ_* profiles of the “in-situ” components or massive galaxies at high redshift. We include: 1) the average μ_* profile of inner component from structure decomposition of massive elliptical galaxies at $z \sim 0$ from Huang et al. (2013b, Blue, dash line); 2) the average μ_* profile of massive galaxies at $1.0 < z < 1.5$ using HST observations from Patel et al. (2013, Yellow, dash line); 3) the average μ_* profile of the “in-situ” stellar components in simulated massive halos from Cooper et al. (2013, Cyan, dotted line); 4) the μ_* profile of the very massive cD galaxy at $z \sim 1.1$ discovered by Liu et al. (2013, Purple, dash line) in the Hubble Ultra-Deep Field.

cesses at high redshift. Later, after the active star formation is quenched in these massive systems, their mass assembly history becomes dominated by accretions of satellites. Based on the prediction of merger tree and current understanding of satellite population around massive galaxies, most these merging events are likely to be minor ones, and without involving much gas dissipation. Since such minor, dry merger basically redistributes stars onto the outer envelope of the central galaxy, it becomes the most promising solution to the “size-evolution” puzzle. However, it raises additional questions at the same time. The most pressing one would be the expected “environmental”-dependence of structures of massive central galaxies. As minor merger is expected to be more frequent in denser environment, the mass assembly history and M_* distribution of central galaxies should show dependence on M_{halo} or even other properties of the host halo. For instance, centrals in more and less massive halos could have different slopes and/or scatters in their mass-size relation (e.g. REF). Yet, no clear evidence of such dependence has been found. In this work, taking advantage of the deep photometry from the HSC survey and looking into the detailed μ_* profiles, we clearly see evidence that the **structure of massive central galaxies, both the inner and outer parts, does show dependence on the halo mass**. Here, we briefly discuss the physical causes of this dependence, potential caveats, and more scientific implications.

Firstly, the comparisons of the μ_* profiles suggest that M_{halo} does not play a central role in shaping the structure of massive central galaxies. It appears that massive central

galaxies at $\log(M_*/M_\odot) \geq 11.5$ were shaped by same physical processes in more and less massive halos. At both fixed $M_{*,100\text{kpc}}$ and $M_{*,10\text{kpc}}$, centrals from cluster-level halos do not form a unique population. Instead, their individual μ_* profiles greatly overlap with the ones in halos of small group. At similar $M_{*,100\text{kpc}}$, even their median μ_* profiles only show quite subtle differences. For the cenHighMh sample, this is similar to the results of (Zhao et al. 2015) that a considerable fraction of nearby BCGs (34%) does not fall into the “cD” class. From the smooth distributions of μ_* profiles on Fig.6 and Fig.9, it is even harder to draw a clear difference between “cD” galaxy and “normal elliptical”.

At the same time, **the M_{halo} -dependence we found do fit the expectations of the “two-phase” scenario at first glance**. For central galaxies with similar stellar mass at the end of the first phase, their subsequent, accretion-dominated mass assembly naturally relates to M_{halo} , which determines the number and mass distributions of satellites. Therefore, centrals of more massive halos should accumulate more extended stellar envelope during the second phase, exactly as we find in the μ_* profile comparison of the $M_{*,10\text{kpc}}$ -matched samples (see Fig.9). Under the “two-phase” formation scenario, the stellar content of massive galaxies can be broadly separated into the “in-situ” and “accreted” components. At fixed $M_{*,100\text{kpc}}$, the differences of median μ_* profiles could reflect different relative fraction of these two components. Recent simulations indicate that (1) the fraction of accreted stars could have a steep correlation with total stellar mass; (2) for $\log(M_*/M_\odot) \geq 11.5$ galaxies, the accreted component starts to dominate within the R_e . Given that (1) the “transition radius” between the two median profiles is around 15–20 kpc (see Fig.6); and (2) the differences become more significant at higher mass end, it is likely the M_{halo} -dependence of structure at fixed total stellar mass is driven by the higher fraction of accreted stars in more massive halos. To confirm this inference, in Fig.14, we compare the median μ_* profiles of the $M_{*,100\text{kpc}}$ -matched cenHighMh and cenLowMh samples at $11.5 \leq \log(M_*/M_\odot) < 11.7$ with the median profiles of (1) massive ETGs at $1.0 < z < 1.5$ that are considered the progenitors of $\sim 10^{11.5} M_\odot$ ETGs at $z = 0$ (Patel et al. 2013). After this redshift range, their mass growth should be dominated by mergers. (2) inner components of $z = 0$ $10^{11.4} M_\odot$ ellipticals from 2-D decomposition (Huang et al. 2013b). (Huang et al. 2013a) showed that these structures are quite similar to the compact progenitors at higher redshift in many aspects. (3) the “in-situ” components of simulated galaxies in massive halo of (Cooper et al. 2013) using particle-tagging technique (the inner few kpc is quite uncertain due to the resolution). Regardless the small difference in median M_* and details in M_*/L_* estimates, the comparison first confirms that $M_{*,10\text{kpc}}$ is indeed not a bad proxy of the in-situ mass; meanwhile, it also highlights that structural difference between cenHighMh and cenLowMh are driven by region that is not dominated by “in-situ” stars. Since most of these samples in comparison are not as extreme as the massive cenHighMh galaxies, we also compare with a uniquely massive BCG at high redshift: a $10^{11.4} M_\odot$ BCGs with distinctive envelope at $z \sim 1.1$ (Liu et al. 2013). It is interesting to see that its μ_* profile follows the median profile of cenHighMh nicely until 20 kpc; then it becomes much steeper in the outskirt. This is quite consistent with the expectation that the inner part of the BCGs should be well developed at $z \sim 1$, but the extended stellar envelope is still assembling.

Also, it is worth noting that the relative flatten inner μ_* profile of `cenHighMh` at fixed $M_{*,100\text{kpc}}$ could be an interesting feature, although we currently lack of the resolution to investigate region ≤ 3 kpc. It is known that major-merger induced coalesce of super-massive black holes (SMBHs) can create flattened inner profile (e.g. ?), and recent discoveries of massive BCGs with very large core (a few kpc; e.g. Postman et al. 2012; López-Cruz et al. 2014) further complicate the picture. On Fig.13, there are a few `cenHighMh` galaxies with quite low $M_{*,10\text{kpc}}$ at high $M_{*,100\text{kpc}}$ end. After examining their images, we conclude the low $M_{*,10\text{kpc}}$ is not caused by problematic photometry or exceptionally bad seeing; they could also be massive BCGs with very flattened inner μ_* profiles. Besides the SMBH-merger theory, strong adiabatic expansion induced by strong AGN feedback was proposed to modify the inner mass distribution (e.g. ?). The potential impact of these processes to massive galaxies, and their dependence on halo mass would be an interesting topic to investigate in the future.

As a start, we only focused on the 1-D μ_* profile derived from *i*-band image. We should not forget that the multi-band, 2-D HSC images of these massive galaxies actually contain much more useful information, particularly the shapes and colors of different stellar components. Strictly speaking, to extract these information reliably, we need to rely on better background subtraction and 2-D modelling method. But, as a motivation, we show initial results from 1-D analysis in Fig.15. The ellipticity profile is extracted from `Ellipse` run on *i*-band image with free geometric parameters. After reducing the *g*- and *r*-band images of our galaxies in consistent way with the *i*-band ones, we simply apply the *i*-band isophotes to images in these two bands without matching the seeing to extract color profiles. All the color profiles are corrected for Galactic extinction and *k*-correction using `iSEDFit` results. We show the median ellipticity, $g-r$, and $g-i$ color profiles of the $M_{*,100\text{kpc}}$ -matched ($M_{*,10\text{kpc}}$ -matched) samples of `cenHighMh` and `cenLowMh` galaxies on the left (right) panel; and also compare them with median profiles from stacking analysis of SDSS galaxies with similar M_* (La Barbera et al. 2010; Tal & van Dokkum 2011; D’Souza et al. 2014) excluding the inner and outer regions affected by seeing and uncertainty of background subtraction. For the $M_{*,100\text{kpc}}$ -matched samples on the left, we notice that the median ellipticity profiles follow the stacked ones well between 5 to 30–50 kpc, but are not plateaued at larger radius. Since they are the median of individually measured ellipticity profiles, they do not suffer the systematics in stacking analysis, and are better at reflecting the intrinsic profiles. In consistent with the 2-D decomposition results in (Huang et al. 2013b), the projected M_* distributions in massive galaxies become increasingly elongated at larger radius. We notice no significant difference between the `cenHighMh` and `cenLowMh` samples, except for maybe some hints that centrals in more massive halos becomes slightly more elliptical at very large radius. For the median color profiles, we see shallow and negative gradients of both $g-r$ and $g-i$ colors as expected. More importantly, the `cenHighMh` and `cenLowMh` samples show very consistent color gradients, which confirms that using average color to derive M_*/L_* of both samples will not bias the comparison of μ_* profiles. Without conversion between the HSC and SDSS filter systems, our median color profiles appear to be little steeper than the stacked ones from SDSS. The exactly cause of this difference is not clear, although it could also be due to the systematics in the stacking process. As for the $M_{*,10\text{kpc}}$ -matched samples on the right, it becomes very clear

that the extended envelopes hosted by `cenHighMh` galaxies have much higher ellipticity, and redder $g-i$ colors than the outskirts of `cenLowMh` ones at similar $M_{*,10\text{kpc}}$. All these preliminary results point out that, by including these information into consideration, we will have a more complete view of the connection between halo/environment and structure of massive central galaxies.

In the end, we want to emphasize once more **the importance of deep image and appropriate method of photometry in studying the structure and assembly history of galaxies**. With the help of deep HSC images, we reliably reveal the extended stellar structures around large sample of massive central galaxies out to more than 100 kpc. And, using model-independent method, we found that (1) previous de Vaucouleur or single-Sérsic modeling method on shallower SDSS images underestimates the total mass of massive galaxies; (2) even using deep HSC images, photometric method like `cModel` also tends to underestimate the mass. For these massive central galaxies, their extended mass distributions are simply beyond the capability of the simply modeling method. In addition, since the slope and mass contribution of the outer envelope depend on not only the total stellar mass, but also likely the halo mass. Applying the same oversimplified model to galaxies across a large range of mass and environment could result in both underestimated and biased mass estimates that can stop us getting accurate stellar mass function at the high-mass end and studying potential environmental dependence of structures. Moreover, these results also raise crucial questions like: **What is the definition of “total” stellar mass of galaxy? And, what is the most informative definition of stellar mass in the studies of galaxy evolution?**. In this work, we choose mass enclosed by different, but fixed physical apertures, and find promising scientific applications for massive galaxies. But, we recognize that they may not be the best choice. For instance, central galaxies of massive halos like BCGs are known to be surrounded by diffuse stellar component that does not follow the potential of the central galaxy (the intra-cluster light, or ICL; e.g. REF). In theory, it can contribute a large amount of stellar mass out to very large radius (e.g. REF). Using the definition of $M_{*,100\text{kpc}}$, we can not separate the potential contribution of ICL in our `cenHighMh` galaxies; and this could make complicate the discussion of environmental dependence. Since most of the `cenHighMh` galaxies in our sample belong to low-mass cluster like the Virgo or Fornax, we do not expect the ICL component can makes a smooth and significant contribution to the μ_* profiles (e.g. REF). Even removing all `cenHighMh` galaxies in $\lambda > 40$ clusters will not change our findings. However, it is still important to ask whether should we include the ICL when estimating the mass of central galaxies in massive halos. And, if the answer is no, which is the best way to separate the ICL component? In literature, most works studied ICL by subtracting the model for inner part of the central galaxy (e.g. REF). As we show in this work, when extended stellar envelopes are revealed around massive galaxies in large range of stellar and halo mass, we may have to reconsider this approach.

7. SUMMARY AND FUTURE PLANS

In this work, we use the deep *i*-band images from the Subaru HSC survey to study the role played by halo mass in determining the mass assembly history and stellar structures of very massive galaxies—the most impressive outcomes of the hierarchical formation process. We map the stellar mass dis-

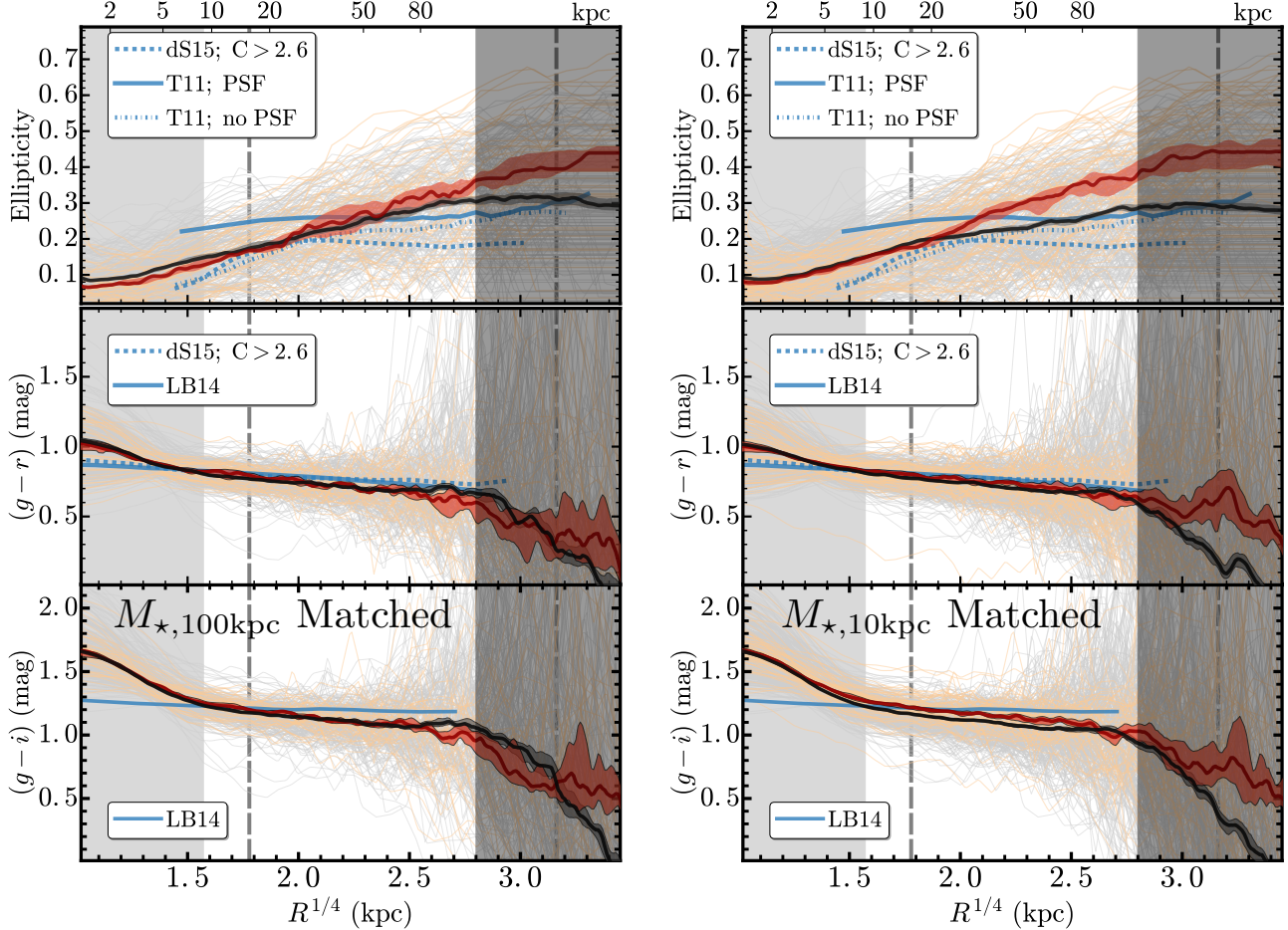


FIG. 15.— Comparisons of the radial profiles for ellipticity and optical colors for $M_{*,100\text{kpc}}$ -matched (left figure) and $M_{*,10\text{kpc}}$ -matched (right figure) of cenHighMh (orange-red) and cenLowMh (grey-black) samples. The formats are very similar to the figure for μ_* profile (e.g. right figure of Fig. ???. On each side, from top to bottom, we show the elliptical profile, and the color profile using $g-r$ and $g-i$ color. Since the individual profile of these properties has very large uncertain in the outskirt, we block the region at large radii where we think the median profiles are still unreliable using a dark, shaded box. We also compare these results with previous results based on SDSS images. They are: 1) Ellipticity profile of stacked image of red galaxies at $z \sim 0.4$ from Tal & van Dokkum (2011), with and without PSF correction (solid and dotted blue lines on top panel); 2) Ellipticity and $g-r$ color profiles from stacking analysis of nearby massive galaxies with high concentration index ($C > 2.6$) in D'Souza et al. (2014, blue dash lines on the top and middle panels); 3) average $g-r$ and $g-i$ color profiles for a large sample of nearby elliptical galaxies in La Barbera et al. (2010, blue, solid lines on the middle and bottom panels).

tributions of a large sample of massive central galaxies at $0.3 < z < 0.5$ out to > 100 kpc. With the help of this impressive dataset, we uncover the very extended stellar envelope around massive central galaxies with great accuracy. We also reveal that, the “total” M_* of massive galaxies can be significantly underestimated if shallow image and/or inappropriate model is used, which can lead to systematics in the study of stellar mass function and other important topics.

More importantly, we discover subtle, but systematic, and robust structural differences in massive galaxies that depend on M_{halo} through comparisons of their μ_* profiles. On average, at fixed M_* within 100 kpc, the massive central galaxies in more massive ($M_{200,m} \gtrsim 1.6 \times 10^{14} M_\odot$) halos show shallower inner μ_* profile within $\sim 15\text{-}20$ kpc, and a more prominent outer envelope comparing to the ones in less massive ($M_{200,c} \gtrsim 8.7 \times 10^{13} M_\odot$) halos. Also, at the same M_* within inner 10 kpc—a proxy of the M_* assembled through the “in-situ” channel, we show that the ones in more massive halos possess much more extended stellar halos in the outskirts. Such differences are broadly consistent with the prediction of the “two-phase” formation scenario of massive galaxies: the ones in more massive halos have experienced more minor, dry mergers that accumulate more stars at large radius.

Meanwhile, we also suspect the differences in the inner profiles at fixed M_* or M_{halo} may help us understand more about the impact from major merger or AGN feedback. We further suggest that the relation between $M_{*,100\text{kpc}}$ and $M_{*,10\text{kpc}}$ ¹² is potentially interesting in diagnosing the assembly history of massive galaxies and their host halos.

7.1. Future Improvements

These results also highlight the advantages of HSC survey in studying the evolution of massive galaxies. By the finish of this paper, the HSC survey will have already doubled its sky coverage to $\sim 200 \text{ deg}^2$, and can provide a much larger sample of massive central galaxies. At the same time, we will work on better data reduction of HSC images by improving the de-blending in crowded region and the accuracy of background subtraction as they can help provide more reliable SED fitting results, and push the photometric limit toward to even lower surface brightness level.

Right now, we still rely on the redMaPPer catalog from SDSS and spectroscopic redshift from SDSS and BOSS. Run-

¹² or other even better proxies of total M_* and the mass formed in the “in-situ” phase.

ning `redMaPPer` algorithm or similar group/cluster finder using HSC catalogs will greatly help us extend the discussion of halo mass to lower mass and higher redshift regimes. Better identifications and measurements of satellites in massive halos will also open up the possibility to study “environment” within the halo: e.g. Compare the structures of satellites in massive halos and centrals in less massive ones at similar stellar mass.

Another key technical improvement would be to apply carefully designed 2-D photometric modeling to these massive galaxies. Using the same principle in Huang et al. 2013b, we will gradually build up the complexity, and explore different models to fit these massive galaxies better. These 2-D models can help us removing the impact from seeing, and dealing with the uncertainties of sky subtraction, so that we can measure the stellar mass distributions to both smaller and larger radii. Applying these models to multiband images with reasonable constraints (e.g. Huang et al. 2016), we can characterize color gradients, and to achieve better estimates of total stellar mass.

Primarily designed as a cosmological survey, the deep imaging depth and excellent *i*-band seeing of HSC can greatly improve the weak lensing analysis of massive galaxies. Therefore, our next major goal will be to investigate trends between halo properties and galaxy properties by measuring the weak lensing signal for samples binned by properties such as $M_{*,10\text{kpc}}$, $M_{*,100\text{kpc}}$, cluster richness, and magnitude gap. Joining the stellar mass distributions and the weak lensing signals together, we can explore tracers that are sensitive to a range of physical processes (strength and type of AGN feedback, merger rate, typical mass ratio of mergers et al.). To help us have better physical insights, we will directly compare our results with predictions from cosmological hydro-simulations such as Illustris (REF), Eagle (REF), or *Horizon-AGN*.

The Hyper Suprime-Cam (HSC) collaboration includes the astronomical communities of Japan and Taiwan, and Princeton University. The HSC instrumentation and software were developed by the National Astronomical Observatory of Japan (NAOJ), the Kavli Institute for the Physics and Mathematics of the Universe (Kavli IPMU), the University of Tokyo, the High Energy Accelerator Research Organization (KEK), the Academia Sinica Institute for Astronomy and Astrophysics in Taiwan (ASIAA), and Princeton University. Funding was contributed by the FIRST program from Japanese Cabinet Office, the Ministry of Education, Culture, Sports, Science and Technology (MEXT), the Japan Society for the Promotion of Science (JSPS), Japan Science and Technology Agency (JST), the Toray Science Foundation, NAOJ, Kavli IPMU, KEK, ASIAA, and Princeton University.

Funding for SDSS-III has been provided by the Alfred P. Sloan Foundation, the Participating Institutions, the National

Science Foundation, and the U.S. Department of Energy. The SDSS-III web site is <http://www.sdss3.org>. SDSS-III is managed by the Astrophysical Research Consortium for the Participating Institutions of the SDSS-III Collaboration including the University of Arizona, the Brazilian Participation Group, Brookhaven National Laboratory, University of Cambridge, University of Florida, the French Participation Group, the German Participation Group, the Instituto de Astrofísica de Canarias, the Michigan State/Notre Dame/JINA Participation Group, Johns Hopkins University, Lawrence Berkeley National Laboratory, Max Planck Institute for Astrophysics, New Mexico State University, New York University, Ohio State University, Pennsylvania State University, University of Portsmouth, Princeton University, the Spanish Participation Group, University of Tokyo, University of Utah, Vanderbilt University, University of Virginia, University of Washington, and Yale University.

The Pan-STARRS1 Surveys (PS1) have been made possible through contributions of the Institute for Astronomy, the University of Hawaii, the Pan-STARRS Project Office, the Max-Planck Society and its participating institutes, the Max Planck Institute for Astronomy, Heidelberg and the Max Planck Institute for Extraterrestrial Physics, Garching, The Johns Hopkins University, Durham University, the University of Edinburgh, Queen’s University Belfast, the Harvard-Smithsonian Center for Astrophysics, the Las Cumbres Observatory Global Telescope Network Incorporated, the National Central University of Taiwan, the Space Telescope Science Institute, the National Aeronautics and Space Administration under Grant No. NNX08AR22G issued through the Planetary Science Division of the NASA Science Mission Directorate, the National Science Foundation under Grant No. AST-1238877, the University of Maryland, and Eotvos Lorand University (ELTE).

This paper makes use of software developed for the Large Synoptic Survey Telescope. We thank the LSST Project for making their code available as free software at <http://dm.lsstcorp.org>.

This research made use of: `STSCI PYTHON`, a general astronomical data analysis infrastructure in Python. `STSCI PYTHON` is a product of the Space Telescope Science Institute, which is operated by AURA for NASA; `SciPy`, an open source scientific tools for Python (Jones et al. 2001); `NumPy`, a fundamental package for scientific computing with Python (Walt et al. 2011); `Matplotlib`, a 2-D plotting library for Python (Hunter 2007); `Astropy`, a community-developed core Python package for Astronomy (Astropy Collaboration et al. 2013); `scikit-learn`, a machine-learning library in Python (Pedregosa et al. 2011); `astroML`, a machine learning library for astrophysics (Vanderplas et al. 2012); `IPython`, an interactive computing system for Python (Pérez & Granger 2007); `sep` Source Extraction and Photometry in Python (Barbary et al. 2015); `palettable`, color palettes for Python; `emcee`, Seriously Kick-Ass MCMC in Python.

REFERENCES

- Aihara, H., Allende Prieto, C., An, D., et al. 2011, *ApJS*, 193, 29
 Alam, S., Albareti, F. D., Allende Prieto, C., et al. 2015, *ApJS*, 219, 12
 Annis, J., Soares-Santos, M., Strauss, M. A., et al. 2014, *ApJ*, 794, 120
 Astropy Collaboration, Robitaille, T. P., Tollerud, E. J., et al. 2013, *A&A*, 558, A33
 Axelrod, T., Kantor, J., Lupton, R. H., & Pierfederici, F. 2010, in Proc. SPIE, Vol. 7740, Software and Cyberinfrastructure for Astronomy, 774015
 Bai, L., Yee, H. K. C., Yan, R., et al. 2014, *ApJ*, 789, 134
 Barbary, Boone, & Deil. 2015, sep: v0.3.0
 Behroozi, P. S., Wechsler, R. H., & Conroy, C. 2013, *ApJ*, 770, 57
 Bellstedt, S., Lidman, C., Muzzin, A., et al. 2016, *MNRAS*, 460, 2862
 Bernardi, M., Meert, A., Sheth, R. K., et al. 2016a, ArXiv e-prints
 —. 2016b, *MNRAS*, 455, 4122
 —. 2013, *MNRAS*, 436, 697
 Blanton, M. R., Kazin, E., Muna, D., Weaver, B. A., & Price-Whelan, A. 2011, *AJ*, 142, 31
 Bosch, J. in prep., In preparation
 Bruzual, G., & Charlot, S. 2003, *MNRAS*, 344, 1000

- Bundy, K., Leauthaud, A., Saito, S., et al. 2015, ApJS, 221, 15
- Calzetti, D., Armus, L., Bohlin, R. C., et al. 2000, ApJ, 533, 682
- Cappellari, M., McDermid, R. M., Alatalo, K., et al. 2012, Nature, 484, 485
- . 2013, MNRAS, 432, 1862
- Chabrier, G. 2003, PASP, 115, 763
- Conroy, C., & Gunn, J. E. 2010a, FSPS: Flexible Stellar Population Synthesis, Astrophysics Source Code Library
- . 2010b, ApJ, 712, 833
- Conroy, C., & van Dokkum, P. G. 2012, ApJ, 760, 71
- Cooper, A. P., D'Souza, R., Kauffmann, G., et al. 2013, MNRAS, 434, 3348
- Cooper, A. P., Cole, S., Frenk, C. S., et al. 2010, MNRAS, 406, 744
- Driver, S. P., Hill, D. T., Kelvin, L. S., et al. 2011, MNRAS, 413, 971
- D'Souza, R., Kauffmann, G., Wang, J., & Vegetti, S. 2014, MNRAS, 443, 1433
- D'Souza, R., Vegetti, S., & Kauffmann, G. 2015, MNRAS, 454, 4027
- Eisenstein, D. J., Weinberg, D. H., Agol, E., et al. 2011, AJ, 142, 72
- Falcón-Barroso, J., Sánchez-Blázquez, P., Vazdekis, A., et al. 2011, A&A, 532, A95
- Farahi, A., Evrard, A. E., Rozo, E., Rykoff, E. S., & Wechsler, R. H. 2016, MNRAS, 460, 3900
- Foreman-Mackey, D., Hogg, D. W., Lang, D., & Goodman, J. 2013, PASP, 125, 306
- Ho, L. C., Li, Z.-Y., Barth, A. J., Seigar, M. S., & Peng, C. Y. 2011, ApJS, 197, 21
- Huang, S., Ho, L. C., Peng, C. Y., Li, Z.-Y., & Barth, A. J. 2013a, ApJ, 768, L28
- . 2013b, ApJ, 766, 47
- . 2016, ApJ, 821, 114
- Huertas-Company, M., Shankar, F., Mei, S., et al. 2013, ApJ, 779, 29
- Hunter, J. D. 2007, Computing In Science & Engineering, 9, 90
- Inagaki, T., Lin, Y.-T., Huang, H.-J., Hsieh, B.-C., & Sugiyama, N. 2015, MNRAS, 446, 1107
- Jones, E., Oliphant, T., Peterson, P., et al. 2001, SciPy: Open source scientific tools for Python, [Online; accessed 2016-09-30]
- Jurić, M., Kantor, J., Lim, K., et al. 2015, ArXiv e-prints
- Kauffmann, G., Heckman, T. M., White, S. D. M., et al. 2003, MNRAS, 341, 54
- Kelvin, L. S., Driver, S. P., Robotham, A. S. G., et al. 2012, MNRAS, 421, 1007
- Kormendy, J., Fisher, D. B., Cornell, M. E., & Bender, R. 2009, ApJS, 182, 216
- Kravtsov, A., Vikhlinin, A., & Meshcheryakov, A. 2014, ArXiv e-prints
- La Barbera, F., De Carvalho, R. R., De La Rosa, I. G., et al. 2010, AJ, 140, 1528
- La Barbera, F., Ferreras, I., de Carvalho, R. R., et al. 2012, MNRAS, 426, 2300
- Lauer, T. R., Gebhardt, K., Faber, S. M., et al. 2007, ApJ, 664, 226
- Lawrence, A., Warren, S. J., Almaini, O., et al. 2007, MNRAS, 379, 1599
- Leauthaud, A., Tinker, J., Bundy, K., et al. 2012, ApJ, 744, 159
- Leauthaud, A., Bundy, K., Saito, S., et al. 2016, MNRAS, 457, 4021
- Li, Z.-Y., Ho, L. C., Barth, A. J., & Peng, C. Y. 2011, ApJS, 197, 22
- Liske, J., Baldry, I. K., Driver, S. P., et al. 2015, MNRAS, 452, 2087
- Liu, F. S., Guo, Y., Koo, D. C., et al. 2013, ApJ, 769, 147
- López-Cruz, O., Afonso, C., Birkshaw, M., et al. 2014, ApJ, 795, L31
- Lupton, R., Blanton, M. R., Fekete, G., et al. 2004, PASP, 116, 133
- Magnier, E. A., Schlafly, E., Finkbeiner, D., et al. 2013, ApJS, 205, 20
- Meert, A., Vikram, V., & Bernardi, M. 2015, MNRAS, 446, 3943
- Miyazaki, S., Komiyama, Y., Nakaya, H., et al. 2012, in Proc. SPIE, Vol. 8446, Ground-based and Airborne Instrumentation for Astronomy IV, 84460Z
- Moustakas, J., Coil, A. L., Aird, J., et al. 2013, ApJ, 767, 50
- Oke, J. B., & Gunn, J. E. 1983, ApJ, 266, 713
- Park, C., Choi, Y.-Y., Vogeley, M. S., et al. 2007, ApJ, 658, 898
- Patel, S. G., van Dokkum, P. G., Franx, M., et al. 2013, ApJ, 766, 15
- Pedregosa, F., Varoquaux, G., Gramfort, A., et al. 2011, Journal of Machine Learning Research, 12, 2825
- Pérez, F., & Granger, B. E. 2007, Computing in Science and Engineering, 9, 21
- Postman, M., Lauer, T. R., Donahue, M., et al. 2012, ApJ, 756, 159
- Ricciardelli, E., Vazdekis, A., Cenarro, A. J., & Falcón-Barroso, J. 2012, MNRAS, 424, 172
- Rozo, E., & Rykoff, E. S. 2014, ApJ, 783, 80
- Rozo, E., Rykoff, E. S., Bartlett, J. G., & Melin, J.-B. 2015a, MNRAS, 450, 592
- Rozo, E., Rykoff, E. S., Becker, M., Reddick, R. M., & Wechsler, R. H. 2015b, MNRAS, 453, 38
- Rykoff, E. S., Rozo, E., Busha, M. T., et al. 2014, ApJ, 785, 104
- Salpeter, E. E. 1955, ApJ, 121, 161
- Sánchez-Blázquez, P., Peletier, R. F., Jiménez-Vicente, J., et al. 2006, MNRAS, 371, 703
- Saro, A., Bocquet, S., Rozo, E., et al. 2015, MNRAS, 454, 2305
- Savorgnan, G., Graham, A. W., Marconi, A., et al. 2013, MNRAS, 434, 387
- Schlafly, E. F., & Finkbeiner, D. P. 2011, ApJ, 737, 103
- Schlafly, E. F., Finkbeiner, D. P., Jurić, M., et al. 2012, ApJ, 756, 158
- Simet, M., McClintock, T., Mandelbaum, R., et al. 2016, ArXiv e-prints
- Tal, T., & van Dokkum, P. G. 2011, ApJ, 731, 89
- Taylor, E. N., Hopkins, A. M., Baldry, I. K., et al. 2011, MNRAS, 418, 1587
- Tony, J. L., Stubbs, C. W., Lykke, K. R., et al. 2012, ApJ, 750, 99
- van Uitert, E., Cacciato, M., Hoekstra, H., et al. 2016, MNRAS, 459, 3251
- Vanderplas, J., Connolly, A., Ivezić, Ž., & Gray, A. 2012, in Conference on Intelligent Data Understanding (CIDU), 47–54
- Walcher, J., Groves, B., Budavári, T., & Dale, D. 2011, Ap&SS, 331, 1
- Walt, S. v. d., Colbert, S. C., & Varoquaux, G. 2011, Computing in Science and Engg., 13, 22
- Wellons, S., Torrey, P., Ma, C.-P., et al. 2016, MNRAS, 456, 1030
- Yang, X., Mo, H. J., van den Bosch, F. C., et al. 2007, ApJ, 671, 153
- Zhao, D., Aragón-Salamanca, A., & Conselice, C. J. 2015, MNRAS, 448, 2530

APPENDIX

A. EXTRACTION OF 1-D SURFACE BRIGHTNESS PROFILE

B. ESTIMATE AVERAGE M_*/L_* USING `ISEDFIT`

We adopt flat distribution between 0.5 to 14.0 Gyrs as prior for the look-back time when the star formation turned on. The exponential delayed time-scale (τ) is allowed to change between 0.1 to 3.0 with equal probability. The chance of random star burst is set at 0.2 for every 2 Gyrs. The duration of the star burst is drawn from a logarithmic distribution between 0.03 to 0.3 Gyr; and the mass fraction formed in the burst is from a logarithmic distribution between 0.01 and 1.0.

In principle, these choices of priors could leave systematic effects in the estimate of stellar mass (e.g. [Bernardi et al. 2016a](#)). For low- z massive ETGs like the ones in our sample, the details form of SFH, importance of random star burst, and the dust extinction should not be major concern. However, the choices of stellar population models and IMF can still change the results systematically. More discussions on this can be found in Appendix A. In short:

- Both FSPS+MILES and BC03 ([Bruzual & Charlot 2003](#)) models still have difficulties recovering the optical color involving filters at the red end (e.g $i-Y$), which could relate to the challenge for modern stellar population models to reproduce the optical color-color relation of red-sequence galaxies (e.g. [Ricciardelli et al. 2012](#)), or the shallower photometry of HSC-Y band data.
- The BC03 provides slightly better overall χ^2 and systematically smaller M_* than the FSPS+MILES models. However, it is possible that the BC03 model tends to underestimate the M_*/L_* for a fraction of them as the estimate stellar age is

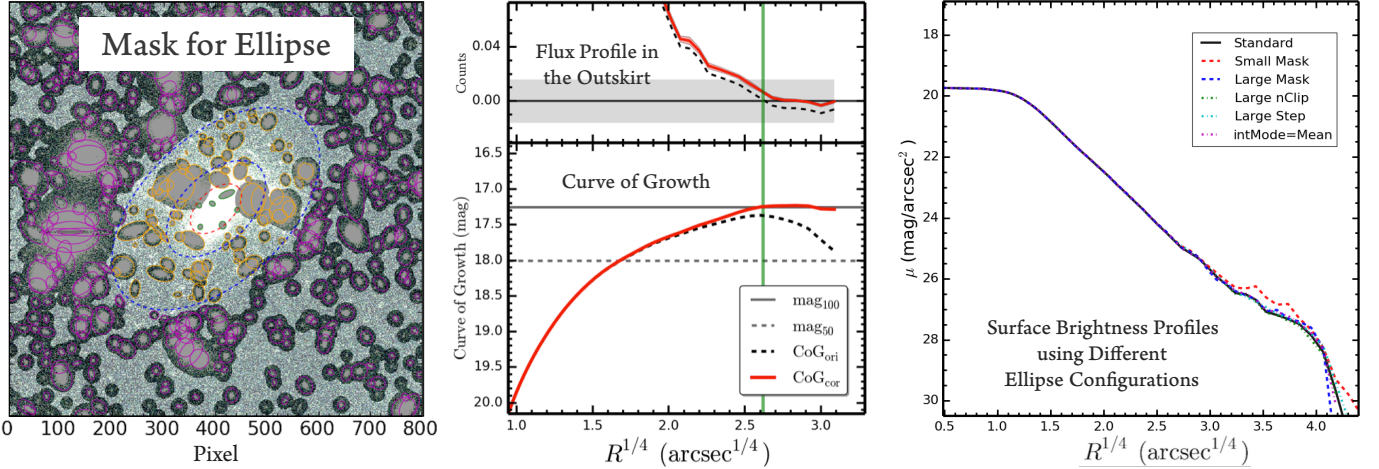


FIG. A1.— **Left:** Example of the object-mask built for the `Ellipse` run for a typical massive galaxy in the sample. All the shaded regions are masked out. The three dash lines (red, inner one and two blue ones) around the target at the center outlines the three radius we defined using the flux radius of the target. We increase the mask size for objects detected in different regions separated by these apertures (which are outlined by solid, elliptical apertures with different colors) using slightly different criteria. **Middle:** The flux profile that is zoomed into the near-zero flux range (top panel), and the curve-of-growth of the magnitude for the example massive galaxy. To highlight the importance of correcting sky background, we show the profiles using both images with (red, solid line) and without (black, dash line) ad-hoc background correction. On the top panel, besides the horizontal line that highlights the zero flux level, we also show the uncertainty of the sky background estimate via grey-shaded region. On the bottom panel, two horizontal lines indicate the magnitudes corresponding to total (solid) and half flux (dash) using the background-corrected profile. **Right:** compare the 1-D surface brightness profiles for the same example galaxy extracted using different mask (smaller masking region: red, dash line; larger masks: blue, dash line), or different `Ellipse` settings (more aggressive pixel-clipping: cyan, dash line; larger step in radius: green, dash line; using mean flux along the isophote instead of median: purple, dash line) with the one using the default configuration (black, solid line).

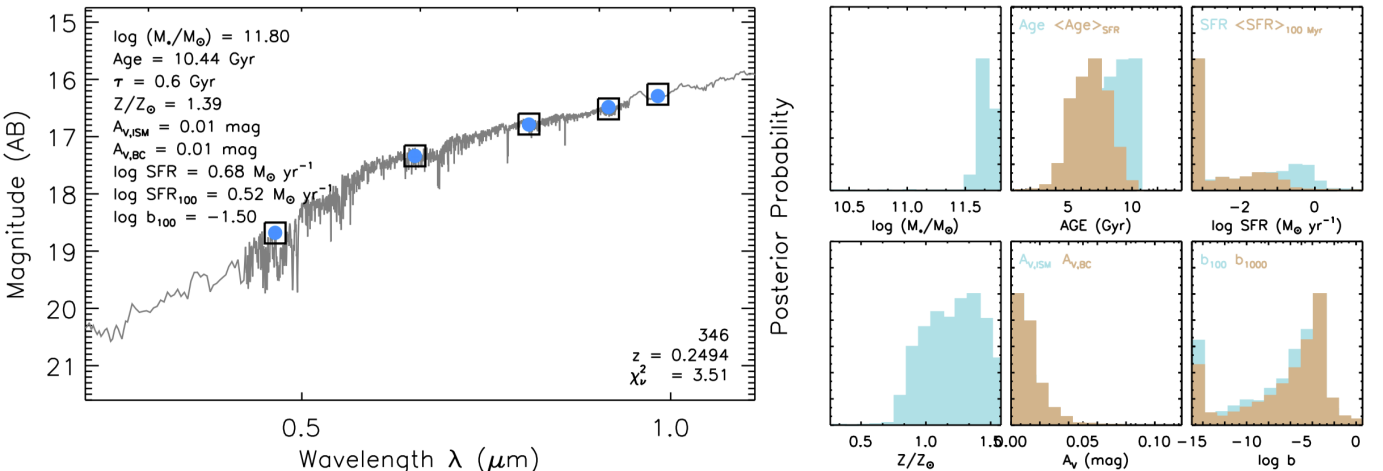


FIG. B1.— Left: example output figure from `iSEDFit` that shows the SED fitting results. The open-boxes show the observed fluxes in 5-band, and the solid, blue-dots show the best-fitted results, along with the high-resolution spectrum for this model reconstructed using the synthetic spectra from `FSPS`. Top-left corner shows the best-fit stellar population parameters, and bottom-right corner shows the ID, redshift of this object, and reduced χ^2 of the best-fit model. Right: the Posterior distributions of a few key parameters. From top-left to bottom right are: 1) stellar mass ($\log(M_*/M_\odot)$); 2) age of the population (mass and star-formation rate weighted) in Gyr; 3) star formation rate ($\log SFR (M_\odot/\text{yr})$; instant one and the one averaged over the previous 100 Myr); 4) stellar metallicity (Z/Z_\odot); 5) dust extinction (A_V in mag); 6) birthrate parameter ($\log b$; averaged over previous 100 and 1000 Myr).

unrealistically young for red, massive galaxies. Therefore, we still use the `FSPS+MILES` model as the fiducial one. But, switching to the BC03 model will not change any key result in this work.

3. The usage of Salpeter (1955) IMF results in systematically higher M_* (on average +0.25 dex of $\log(M_*/M_\odot)$). Although there are multiple lines of evidence that favor Salpeter or even more “bottom-heavy” IMF in the most massive ETGs (e.g. Conroy & van Dokkum 2012; Cappellari et al. 2012), we still present the main results using Chabrier IMF to accommodate galaxies with lower M_* in the sample, and to be as consistent as possible with a few other works. Also, the choice of IMF does not impact our results qualitatively.

Besides the priors for stellar population properties, different treatments of the light profile and accuracy of sky background subtraction are also important for the estimate of M_* as they strongly impact the estimate of total luminosity (e.g. Bernardi et al. 2013 and D’Souza et al. 2015). At the depth of SDSS, the default `cModel` photometry is already shown to be not very accurate at high- M_* end (e.g. Meert et al. 2015; Bernardi et al. 2016b) as it does not capture the extended envelope of these galaxies. As for HSC, it is much more challenging for `cModel` to recover the total luminosity of massive ETGs since the stellar envelope

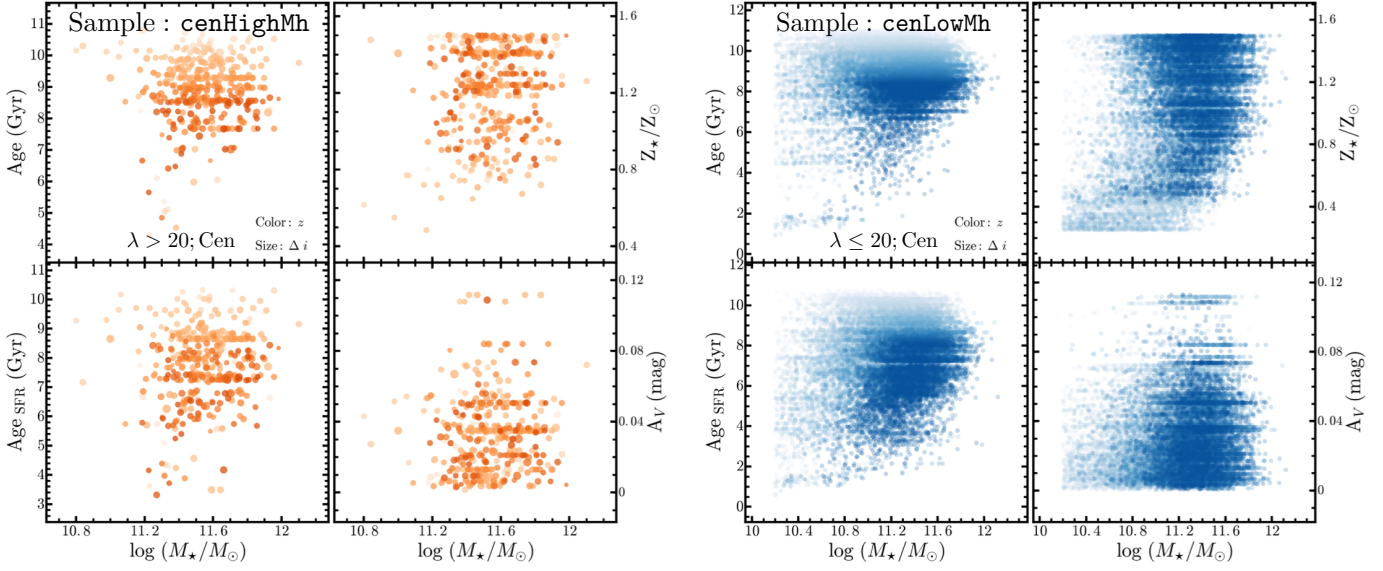


FIG. B2.— Relationships between M_* and certain stellar population parameter using `iSEDFit`. The left figures are for the `cenHighMh` sample, while the right ones are for the `cenLowMh` sample. They are both color-coded using the mass-weighted stellar age. The four stellar population properties shown here are: 1) mass-weighted stellar age in Gyr (top-left); 2) SFR-weighted stellar age in Gyr (bottom-left); 3) mass-weighted stellar metallicity in unit of solar value (top-right); 4) dust extinction value in magnitude (bottom-right).

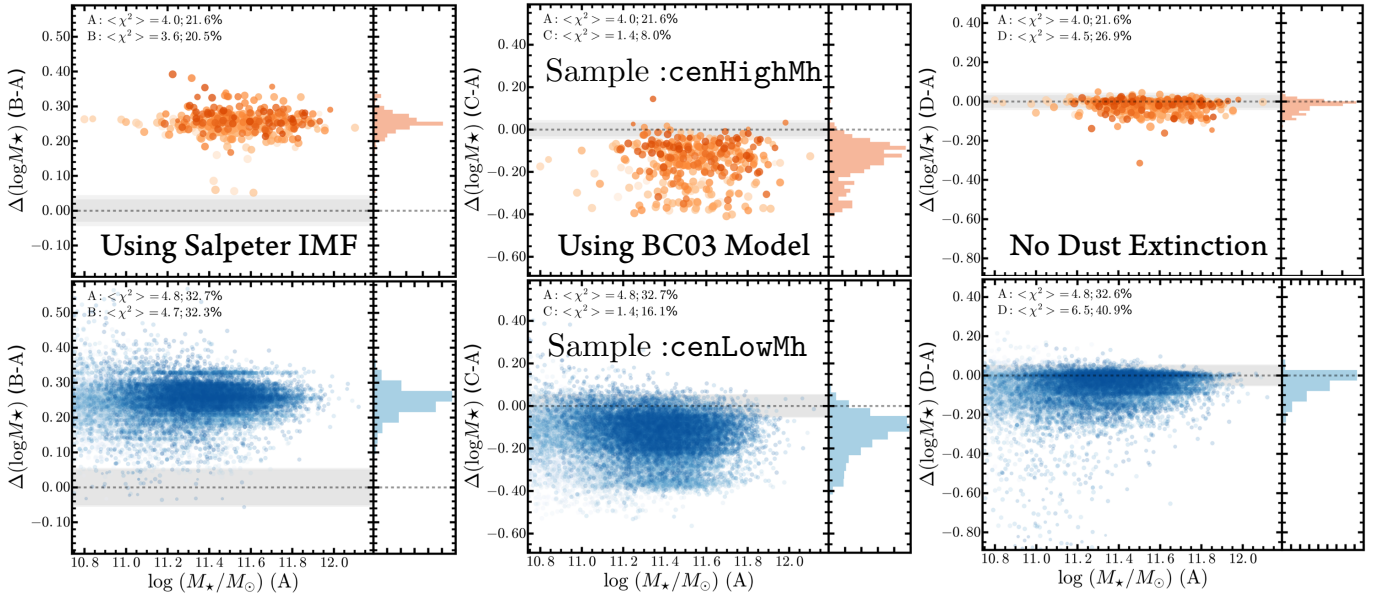


FIG. B3.— Comparisons of M_* estimated by `iSEDFit` using different assumptions. In each figure, we plot the default M_* values against their differences with the results using other models. The top (bottom) row shows comparisons for the `cenHighMh` (`cenLowMh`) sample. The results involved here are labeled: (A): default one; (B): using the Salpeter IMF instead of the Chabrier one (Left column); (C): using the BC03 synthetic population model instead of the FSPS one (Middle column); (D): assume that there is no dust extinction (Right column). On each figure, a horizontal line shows the zero difference level, along with the grey shaded region that highlights the typical uncertainty of the M_* -differences. We also show the histogram of the M_* -differences on the right.

becomes even more extended for neither de Vaucouleur or exponential model to reproduce. However, the HSC cModel under the force-photometry mode can measure **average** color of the galaxy with great accuracy (e.g. Huang et al. in prep.), and provide us a reliable SED to estimate the **average** M_*/L_* . Considering this, we separate the process of estimating the total M_* of massive ETGs in our sample into two steps:

1. Firstly, using the redshift and cModel magnitude in five bands, we derive an initial estimate of the M_* of the galaxy. More importantly, we derive the **average** M_*/L_* in i -band of the galaxy, and use the best-fit SED to provide k -correction to the photometry.
2. In the next section, we will derive better estimate of total M_* using the more accurate total luminosity in i -band from integration of carefully measured 1-D surface brightness profile, and the average M_*/L_* from the SED fitting.

The basic results from `iSEDFit` are summarized in Figure 2, where we compare the relations between initial estimates of M_* and (both luminosity and star formation weighted) stellar age, metallicity, and dust extinction. As expected, most galaxies in our samples are $\log(M_{*,\text{ini}}/M_\odot) \geq 11.2$ massive galaxies that have old age, high metallicity ($1.5 \times Z_\odot$ is the highest metallicity allowed), and low dust extinction. Given that we only have photometry from five optical bands, degeneracies among age, metallicity, and dust extinction are naturally expected. We will not use them for any scientific reason in this work, but to show that they behave reasonably.

C. COMPARISON OF μ_* PROFILES USING M_* FROM THE GAMA SURVEY

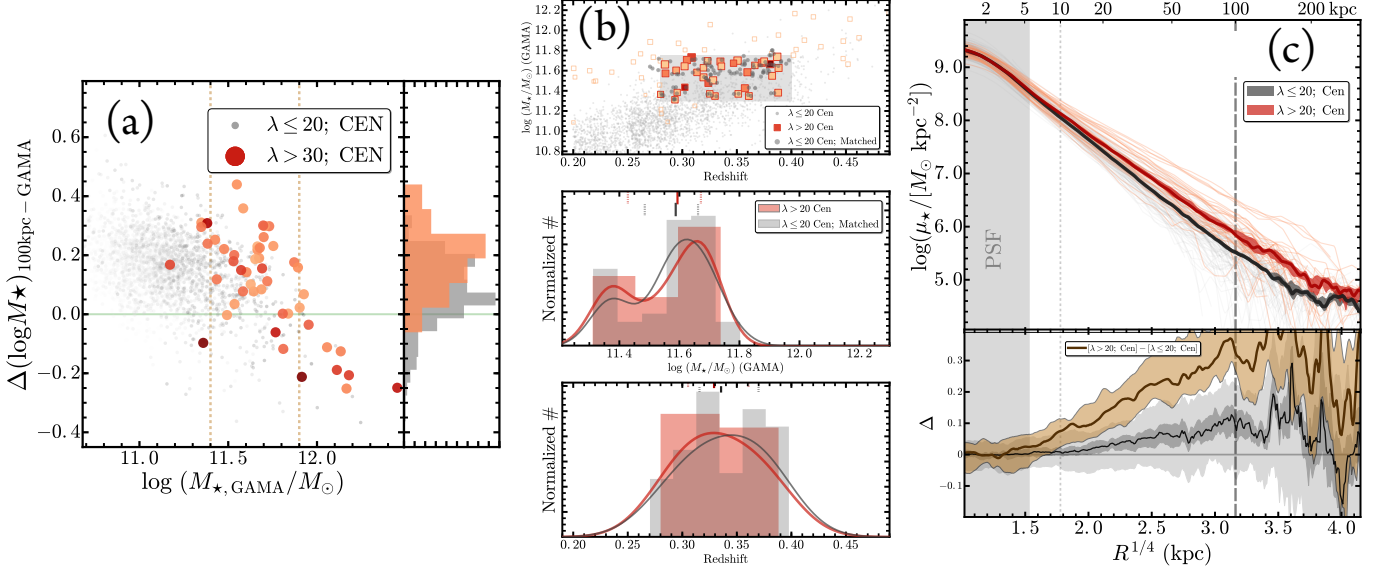


FIG. C1.— **Left:** comparison of M_* estimated by the GAMA survey and the ones in this work for the same galaxies. We plot the $\log(M_{*,\text{GAMA}}/M_\odot)$ against the difference between $\log(M_{*,100\text{kpc}}/M_\odot)$ and $\log(M_{*,\text{GAMA}}/M_\odot)$. The format is very similar to the right panel of Fig. 3, except that we color-code the `cenHighMh` galaxies (orange-red) using the Sérsic index measured by GAMA using `GALFIT` on SDSS image. The two vertical lines highlight the mass range $11.4 \leq \log(M_{*,\text{GAMA}}/M_\odot) < 11.9$ that is used for the comparison later. **Middle and Right figures:** we compare the μ_* profiles of `cenHighMh` (orange-red) and `cenLowMh` (grey-black) galaxies using the samples matched on the $M_*,\text{GAMA}-z$ plane at $11.4 \leq \log(M_{*,\text{GAMA}}/M_\odot) < 11.9$ and $0.28 \leq z < 0.4$. The formats for figure (b) and (c) are very similar to Fig.6.

As the sky coverage of this release greatly overlaps with the GAMA survey, we start the detailed comparison with an external check using the stellar mass estimated by (Taylor et al. 2011). The purpose is still to investigate the impact of deeper photometry on the analysis of structure of massive galaxies. The stellar masses of GAMA galaxies are initially derived through careful optical-SED fitting (BC03 model; Chabrier IMF) using the PSF-matched aperture photometry. Then they were corrected for the total luminosity estimated using single-Sérsic 2-D model to multi-band images (Kelvin et al. 2012). We separate the `cenHighMh` and `cenLowMh` galaxies that also have spec-z and stellar mass in GAMA DR2 (Liske et al. 2015). Most of galaxies in these subsamples have $z < 0.40$.

In Fig. 10, we show the results of matches for subsamples using $M_{*,\text{GAMA}}$. To increase the number of available `cenHighMh` to match, we loosen its selection criteria to $\lambda \geq 20$ and $P_{\text{CEN}} \geq 0.6$. Based on the distributions of the two samples at the $M_*,\text{GAMA}-z$ plane, and their overlapped region, we match them in two bins of $M_{*,\text{GAMA}}$ that have slightly different redshift ranges. For the samples in two $M_{*,\text{GAMA}}$, the matches appear to be very good.

In Fig. 11, we show the individual profiles, median profiles along with their uncertainties derived using 5000 times bootstrap resampling, and the relative difference between the profile of the `cenHighMh` and `cenLowMh` subsamples. It is very clear that, for both mass bins, the `cenHighMh` has a much more extended outer envelope, while its profile inside ~ 10 kpc is very close to the `cenLowMh` one. This is inconsistent with the matched distributions of their “total” stellar mass, and reveals potential issue with the stellar mass estimated by GAMA. We can reproduce very similar results using the luminosity density profiles (with or without k -correction) of these matched samples, which suggests that the main problem does not lie in the estimate of M_*/L_* , but in the measurement of total luminosity using single-Sérsic model. This highlights the importance of deep optical images in studying the structure of massive galaxies.

In cases of these $M_{*,\text{GAMA}}$ -matched samples, the differences of median profiles are very robust.

D. COMPARISONS OF μ_* PROFILES IN DIFFERENT REDSHIFT BINS

As the massive galaxies in our samples span quite a bit in both redshift and $M_{*,100\text{kpc}}$, it is important to evaluate the impact from PSF on the μ_* profiles at different redshift. In Fig.D1, we group the `cenHighMh` and `cenLowMh` galaxies at $11.6 \leq \log(M_{*,100\text{kpc}}/M_\odot) < 11.9$ into two z bins ($0.3 \leq z < 0.4$ and $0.4 \leq z < 0.5$). We did not match the $M_{*,100\text{kpc}}$ distributions in two z bins, so slight difference in average $M_{*,100\text{kpc}}$ can be expected. With the same seeing condition, the μ_* profile of galaxy at higher redshift is more vulnerable to the PSF smearing effect in the center, while suffers more in the outskirt due to

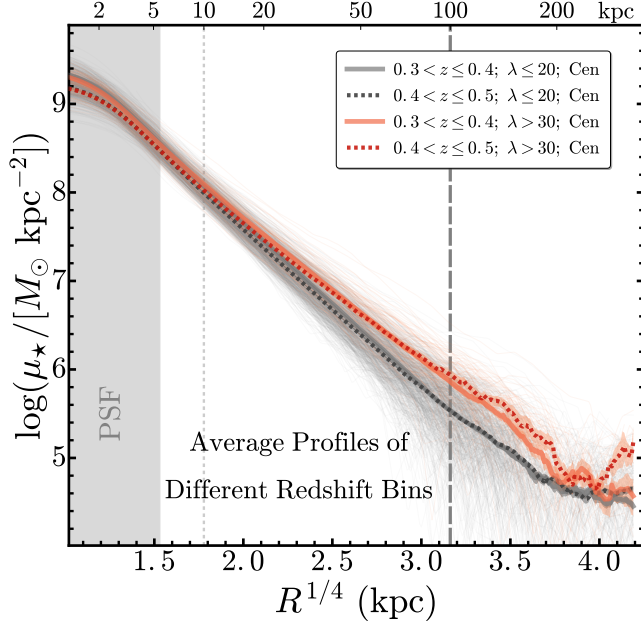


FIG. D1.— Comparison of μ_* profiles of cenHighMh (orange-red) and cenLowMh (grey-black) at $11.6 \leq \log(M_{*,100\text{kpc}}/M_\odot) < 11.9$ in redshift bins of $0.3 \leq z < 0.4$ (solid lines) and $0.4 \leq z < 0.5$ (dash lines). We show the individual profile in the background using much thinner line, and highlight the median profiles using thicker line and darker color. Other formats are exactly the same with the left figure of Fig. 5.

cosmological dimming and background noise. Fig.D1 clearly shows that, although the median profiles of the same sample in two redshift bins follow each other well outside 10 kpc, they start to differ in the central 2-3 kpc as the one from higher redshift bin has more flattened profile due to PSF smearing effect. Meanwhile, we notice that the median profiles of cenHighMh and cenLowMh in the same z bin are very similar to each other in the region affected by seeing. This comparison confirms the radius range that is sensitive to seeing and redshift distribution is well constrained within the grey-shaded area. It also suggests that it is important to match the redshift distributions between samples before we can compare their μ_* profiles or other properties at inner region, as we did in this work. In the outskirts, within 100-150 kpc, we see no difference in the median μ_* profiles caused by redshift distributions. We therefore conclude that it is safe to study the μ_* profile within this radius range for massive galaxies at $z < 0.5$ using HSC images.

TABLE 1
MEDIAN μ_* PROFILES OF MASSIVE GALAXIES IN DIFFERENT STELLAR MASS BINS

R/kpc	μ_* ($\log(M_\odot/\text{kpc}^2)$) for cenHighMh			μ_* ($\log(M_\odot/\text{kpc}^2)$) for cenLowMh			
	$\log \frac{M_{*,100\text{kpc}}}{M_\odot} \in [11.5, 11.7]$			$\log \frac{M_{*,100\text{kpc}}}{M_\odot} \in [11.7, 11.9]$			
	(1)	(2)	(3)	(4)	(5)	(6)	(7)
0.0	$9.30^{+0.02}_{-0.02}$	$9.33^{+0.02}_{-0.02}$	$9.34^{+0.02}_{-0.03}$	$9.36^{+0.00}_{-0.03}$	$9.27^{+0.00}_{-0.00}$	$9.32^{+0.01}_{-0.01}$	
0.5	$9.28^{+0.02}_{-0.02}$	$9.31^{+0.02}_{-0.02}$	$9.32^{+0.03}_{-0.02}$	$9.33^{+0.00}_{-0.00}$	$9.25^{+0.00}_{-0.00}$	$9.30^{+0.01}_{-0.01}$	
0.8	$9.25^{+0.02}_{-0.02}$	$9.28^{+0.02}_{-0.02}$	$9.30^{+0.02}_{-0.02}$	$9.29^{+0.00}_{-0.00}$	$9.22^{+0.00}_{-0.00}$	$9.27^{+0.01}_{-0.01}$	
1.2	$9.22^{+0.02}_{-0.02}$	$9.25^{+0.02}_{-0.02}$	$9.28^{+0.02}_{-0.02}$	$9.24^{+0.00}_{-0.00}$	$9.19^{+0.00}_{-0.00}$	$9.24^{+0.01}_{-0.01}$	
1.5	$9.16^{+0.02}_{-0.01}$	$9.20^{+0.02}_{-0.02}$	$9.24^{+0.02}_{-0.03}$	$9.17^{+0.00}_{-0.00}$	$9.14^{+0.00}_{-0.00}$	$9.20^{+0.01}_{-0.01}$	
1.9	$9.10^{+0.01}_{-0.01}$	$9.14^{+0.02}_{-0.01}$	$9.19^{+0.03}_{-0.03}$	$9.08^{+0.00}_{-0.00}$	$9.08^{+0.00}_{-0.00}$	$9.15^{+0.01}_{-0.01}$	
2.2	$9.03^{+0.01}_{-0.01}$	$9.08^{+0.01}_{-0.01}$	$9.14^{+0.03}_{-0.03}$	$9.00^{+0.00}_{-0.00}$	$9.01^{+0.00}_{-0.00}$	$9.09^{+0.01}_{-0.01}$	
2.5	$8.97^{+0.01}_{-0.01}$	$9.03^{+0.01}_{-0.01}$	$9.10^{+0.02}_{-0.02}$	$8.93^{+0.00}_{-0.00}$	$8.96^{+0.00}_{-0.00}$	$9.04^{+0.01}_{-0.01}$	
2.9	$8.90^{+0.01}_{-0.01}$	$8.97^{+0.01}_{-0.01}$	$9.04^{+0.02}_{-0.02}$	$8.85^{+0.00}_{-0.00}$	$8.89^{+0.00}_{-0.00}$	$8.98^{+0.01}_{-0.01}$	
3.2	$8.83^{+0.01}_{-0.01}$	$8.90^{+0.01}_{-0.01}$	$8.99^{+0.01}_{-0.02}$	$8.77^{+0.00}_{-0.00}$	$8.82^{+0.00}_{-0.00}$	$8.91^{+0.00}_{-0.01}$	
3.6	$8.75^{+0.01}_{-0.01}$	$8.83^{+0.01}_{-0.01}$	$8.93^{+0.01}_{-0.01}$	$8.68^{+0.00}_{-0.00}$	$8.74^{+0.00}_{-0.00}$	$8.84^{+0.01}_{-0.01}$	
4.0	$8.69^{+0.01}_{-0.01}$	$8.78^{+0.01}_{-0.01}$	$8.88^{+0.01}_{-0.01}$	$8.61^{+0.00}_{-0.00}$	$8.69^{+0.00}_{-0.00}$	$8.79^{+0.01}_{-0.01}$	
4.3	$8.63^{+0.01}_{-0.01}$	$8.72^{+0.01}_{-0.01}$	$8.83^{+0.01}_{-0.01}$	$8.55^{+0.00}_{-0.00}$	$8.63^{+0.00}_{-0.00}$	$8.73^{+0.01}_{-0.01}$	
4.7	$8.56^{+0.01}_{-0.01}$	$8.67^{+0.01}_{-0.01}$	$8.78^{+0.01}_{-0.01}$	$8.48^{+0.00}_{-0.00}$	$8.56^{+0.00}_{-0.00}$	$8.68^{+0.01}_{-0.00}$	
6.1	$8.36^{+0.01}_{-0.01}$	$8.48^{+0.01}_{-0.01}$	$8.61^{+0.01}_{-0.01}$	$8.26^{+0.00}_{-0.00}$	$8.36^{+0.00}_{-0.00}$	$8.48^{+0.01}_{-0.00}$	
7.4	$8.20^{+0.01}_{-0.01}$	$8.34^{+0.01}_{-0.01}$	$8.47^{+0.01}_{-0.02}$	$8.09^{+0.00}_{-0.00}$	$8.19^{+0.00}_{-0.00}$	$8.33^{+0.01}_{-0.01}$	
8.8	$8.07^{+0.01}_{-0.01}$	$8.22^{+0.01}_{-0.01}$	$8.36^{+0.02}_{-0.02}$	$7.94^{+0.00}_{-0.00}$	$8.05^{+0.00}_{-0.00}$	$8.20^{+0.01}_{-0.01}$	
10.3	$7.94^{+0.01}_{-0.01}$	$8.10^{+0.01}_{-0.01}$	$8.25^{+0.02}_{-0.03}$	$7.79^{+0.00}_{-0.00}$	$7.91^{+0.00}_{-0.00}$	$8.07^{+0.01}_{-0.01}$	
11.7	$7.82^{+0.01}_{-0.01}$	$8.00^{+0.01}_{-0.01}$	$8.16^{+0.02}_{-0.02}$	$7.66^{+0.00}_{-0.00}$	$7.79^{+0.00}_{-0.00}$	$7.96^{+0.01}_{-0.01}$	
13.0	$7.73^{+0.01}_{-0.01}$	$7.92^{+0.01}_{-0.01}$	$8.08^{+0.02}_{-0.02}$	$7.55^{+0.00}_{-0.00}$	$7.70^{+0.00}_{-0.00}$	$7.87^{+0.01}_{-0.01}$	
14.5	$7.64^{+0.01}_{-0.01}$	$7.84^{+0.02}_{-0.01}$	$8.01^{+0.02}_{-0.02}$	$7.45^{+0.00}_{-0.00}$	$7.60^{+0.00}_{-0.00}$	$7.78^{+0.01}_{-0.01}$	
16.0	$7.55^{+0.02}_{-0.02}$	$7.75^{+0.01}_{-0.01}$	$7.94^{+0.02}_{-0.02}$	$7.34^{+0.00}_{-0.00}$	$7.50^{+0.00}_{-0.00}$	$7.70^{+0.01}_{-0.01}$	
17.3	$7.48^{+0.02}_{-0.02}$	$7.69^{+0.01}_{-0.01}$	$7.88^{+0.02}_{-0.02}$	$7.25^{+0.00}_{-0.00}$	$7.42^{+0.00}_{-0.00}$	$7.63^{+0.01}_{-0.01}$	
18.7	$7.41^{+0.02}_{-0.02}$	$7.62^{+0.02}_{-0.02}$	$7.83^{+0.02}_{-0.02}$	$7.16^{+0.00}_{-0.00}$	$7.34^{+0.00}_{-0.00}$	$7.56^{+0.01}_{-0.01}$	
22.6	$7.23^{+0.02}_{-0.02}$	$7.47^{+0.02}_{-0.02}$	$7.69^{+0.02}_{-0.02}$	$6.94^{+0.00}_{-0.00}$	$7.15^{+0.00}_{-0.00}$	$7.38^{+0.01}_{-0.01}$	
26.1	$7.10^{+0.02}_{-0.02}$	$7.34^{+0.02}_{-0.02}$	$7.58^{+0.02}_{-0.02}$	$6.76^{+0.00}_{-0.00}$	$7.00^{+0.00}_{-0.00}$	$7.25^{+0.01}_{-0.01}$	
30.0	$6.96^{+0.02}_{-0.02}$	$7.22^{+0.02}_{-0.02}$	$7.47^{+0.02}_{-0.02}$	$6.58^{+0.00}_{-0.00}$	$6.84^{+0.00}_{-0.00}$	$7.11^{+0.01}_{-0.01}$	
33.7	$6.84^{+0.02}_{-0.02}$	$7.11^{+0.02}_{-0.02}$	$7.37^{+0.02}_{-0.02}$	$6.42^{+0.01}_{-0.01}$	$6.71^{+0.00}_{-0.00}$	$6.99^{+0.01}_{-0.01}$	
37.8	$6.72^{+0.03}_{-0.02}$	$7.01^{+0.02}_{-0.02}$	$7.27^{+0.03}_{-0.03}$	$6.27^{+0.00}_{-0.00}$	$6.57^{+0.00}_{-0.00}$	$6.87^{+0.01}_{-0.01}$	
41.6	$6.62^{+0.02}_{-0.02}$	$6.92^{+0.02}_{-0.02}$	$7.18^{+0.02}_{-0.02}$	$6.14^{+0.01}_{-0.01}$	$6.46^{+0.00}_{-0.01}$	$6.77^{+0.01}_{-0.01}$	
45.7	$6.50^{+0.03}_{-0.03}$	$6.82^{+0.02}_{-0.02}$	$7.09^{+0.02}_{-0.02}$	$6.01^{+0.01}_{-0.01}$	$6.34^{+0.01}_{-0.00}$	$6.66^{+0.01}_{-0.01}$	
49.3	$6.42^{+0.03}_{-0.03}$	$6.74^{+0.03}_{-0.02}$	$7.02^{+0.02}_{-0.02}$	$5.91^{+0.01}_{-0.01}$	$6.25^{+0.01}_{-0.01}$	$6.57^{+0.01}_{-0.01}$	
53.1	$6.34^{+0.03}_{-0.03}$	$6.67^{+0.03}_{-0.02}$	$6.94^{+0.02}_{-0.02}$	$5.81^{+0.01}_{-0.01}$	$6.15^{+0.01}_{-0.01}$	$6.48^{+0.01}_{-0.01}$	
57.2	$6.25^{+0.03}_{-0.03}$	$6.59^{+0.03}_{-0.03}$	$6.86^{+0.03}_{-0.03}$	$5.71^{+0.01}_{-0.01}$	$6.06^{+0.01}_{-0.01}$	$6.40^{+0.01}_{-0.01}$	
61.5	$6.18^{+0.03}_{-0.03}$	$6.52^{+0.03}_{-0.03}$	$6.78^{+0.03}_{-0.03}$	$5.62^{+0.01}_{-0.01}$	$5.96^{+0.01}_{-0.01}$	$6.31^{+0.01}_{-0.01}$	
65.1	$6.11^{+0.04}_{-0.04}$	$6.46^{+0.03}_{-0.03}$	$6.72^{+0.03}_{-0.03}$	$5.55^{+0.01}_{-0.01}$	$5.89^{+0.01}_{-0.01}$	$6.23^{+0.01}_{-0.01}$	
68.8	$6.02^{+0.04}_{-0.04}$	$6.39^{+0.03}_{-0.03}$	$6.66^{+0.03}_{-0.03}$	$5.48^{+0.01}_{-0.01}$	$5.82^{+0.01}_{-0.01}$	$6.16^{+0.01}_{-0.01}$	
73.7	$5.95^{+0.04}_{-0.05}$	$6.32^{+0.03}_{-0.03}$	$6.58^{+0.03}_{-0.04}$	$5.40^{+0.01}_{-0.01}$	$5.73^{+0.01}_{-0.01}$	$6.07^{+0.01}_{-0.01}$	
78.9	$5.88^{+0.05}_{-0.05}$	$6.24^{+0.03}_{-0.03}$	$6.50^{+0.04}_{-0.04}$	$5.33^{+0.01}_{-0.01}$	$5.65^{+0.01}_{-0.01}$	$5.99^{+0.01}_{-0.01}$	
84.3	$5.79^{+0.06}_{-0.06}$	$6.17^{+0.03}_{-0.03}$	$6.42^{+0.04}_{-0.04}$	$5.26^{+0.01}_{-0.01}$	$5.58^{+0.01}_{-0.01}$	$5.91^{+0.02}_{-0.02}$	
91.2	$5.71^{+0.06}_{-0.06}$	$6.08^{+0.03}_{-0.03}$	$6.31^{+0.05}_{-0.05}$	$5.19^{+0.01}_{-0.01}$	$5.48^{+0.01}_{-0.01}$	$5.81^{+0.02}_{-0.02}$	
98.5	$5.65^{+0.05}_{-0.05}$	$6.00^{+0.03}_{-0.03}$	$6.22^{+0.06}_{-0.07}$	$5.12^{+0.01}_{-0.01}$	$5.40^{+0.01}_{-0.01}$	$5.69^{+0.02}_{-0.02}$	
106.2	$5.55^{+0.06}_{-0.06}$	$5.92^{+0.03}_{-0.03}$	$6.15^{+0.05}_{-0.07}$	$5.05^{+0.01}_{-0.01}$	$5.30^{+0.01}_{-0.01}$	$5.60^{+0.02}_{-0.02}$	
115.7	$5.46^{+0.06}_{-0.06}$	$5.81^{+0.03}_{-0.03}$	$6.08^{+0.04}_{-0.05}$	$4.98^{+0.01}_{-0.02}$	$5.21^{+0.01}_{-0.01}$	$5.51^{+0.02}_{-0.02}$	
123.0	$5.45^{+0.05}_{-0.06}$	$5.72^{+0.04}_{-0.04}$	$6.00^{+0.05}_{-0.05}$	$4.91^{+0.02}_{-0.02}$	$5.16^{+0.01}_{-0.01}$	$5.44^{+0.02}_{-0.02}$	
129.0	$5.43^{+0.05}_{-0.06}$	$5.67^{+0.04}_{-0.04}$	$5.93^{+0.05}_{-0.04}$	$4.85^{+0.02}_{-0.02}$	$5.11^{+0.01}_{-0.01}$	$5.37^{+0.02}_{-0.02}$	
136.8	$5.37^{+0.06}_{-0.06}$	$5.63^{+0.04}_{-0.04}$	$5.82^{+0.06}_{-0.06}$	$4.78^{+0.02}_{-0.02}$	$5.03^{+0.02}_{-0.02}$	$5.29^{+0.02}_{-0.02}$	
145.0	$5.29^{+0.06}_{-0.08}$	$5.57^{+0.04}_{-0.04}$	$5.72^{+0.08}_{-0.08}$	$4.71^{+0.02}_{-0.02}$	$4.96^{+0.02}_{-0.02}$	$5.21^{+0.02}_{-0.03}$	

NOTE. — Median μ_* profiles of massive cenHighMh and cenLowMh galaxies in different M_* bins. Col. (1) Radius in kpc. Col. (2) Median μ_* profile for cenHighMh galaxies with $11.5 \leq \log(M_{*,100\text{kpc}}/M_\odot) < 11.7$. Col. (3) Median μ_* profile for cenHighMh galaxies with $11.7 \leq \log(M_{*,100\text{kpc}}/M_\odot) < 11.9$. Col. (4) Median μ_* profile for cenHighMh galaxies with $11.9 \leq \log(M_{*,100\text{kpc}}/M_\odot) < 12.1$. Col. (5) Median μ_* profile for cenLowMh galaxies with $11.2 \leq \log(M_{*,100\text{kpc}}/M_\odot) < 11.5$. Col. (6) Median μ_* profile for cenLowMh galaxies with $11.5 \leq \log(M_{*,100\text{kpc}}/M_\odot) < 11.7$. Col. (7) Median μ_* profile for cenLowMh galaxies with $11.7 \leq \log(M_{*,100\text{kpc}}/M_\odot) < 11.9$. The full table is available in electronic version.